Contributions of Different Combinations of the IPO and AMO to Recent Changes in Winter East Asian Jets

DANQING HUANG

CMA–NJU Joint Laboratory for Climate Prediction Studies, School of Atmospheric Sciences, Nanjing University, Nanjing, China

AIGUO DAI

Department of Atmospheric and Environmental Sciences, University at Albany, State University of New York, Albany, New York

BEN YANG AND PEIWEN YAN

CMA–NJU Joint Laboratory for Climate Prediction Studies, School of Atmospheric Sciences, Nanjing University, Nanjing, China

JIAN ZHU

State Key Laboratory of Hydrology-Water Resources and Hydraulic Engineering, Hohai University, Nanjing, China

YAOCUN ZHANG

CMA–NJU Joint Laboratory for Climate Prediction Studies, School of Atmospheric Sciences, Nanjing University, Nanjing, China

(Manuscript received 10 April 2018, in final form 8 October 2018)

ABSTRACT

Recent concurrent shifts of the East Asian polar-front jet (EAPJ) and the East Asian subtropical jet (EASJ) in the boreal winter have raised concerns, since they could result in severe weather events over East Asia. However, the possible mechanisms are not fully understood. In this study, the roles of the interdecadal Pacific oscillation (IPO) and the Atlantic multidecadal oscillation (AMO) are investigated by analyzing reanalysis data and model simulations. Results show that combinations of opposite phases of the IPO and AMO can result in significant shifts of the two jets during 1920–2014. This relationship is particularly evident during 1999–2014 and 1979–98 in the reanalysis data. A combination of a negative phase of the IPO (−IPO) and a positive phase of the AMO (+AMO) since the late 1990s has enhanced the meridional temperature gradient and the Eady growth rate and thus westerlies over the region between the two jets, but weakened them to the south and north of the region, thereby contributing to the equatorward and poleward shifts of the EAPJ and EASJ, respectively. Atmospheric model simulations are further used to investigate the relative contribution of −IPO and +AMO to the jet shifts. The model simulations show that the combination of −IPO and +AMO favors the recent jet changes more than the individual −IPO or +AMO. Under a concurrent −IPO and +AMO, the meridional eddy transport of zonal momentum and sensitive heat strengthens, and more mean available potential energy converts to the eddy available potential energy over the region between the two jets, which enhances westerly winds there.

1. Introduction

In the upper troposphere and lower stratosphere throughout the year, there are two branches of narrow and strong jets over East Asia with severe wind shear and strong atmospheric baroclinicity. They are referred to as the East Asian polar-front jet (EAPJ) and the East Asian subtropical jet (EASJ; e.g., Zou et al. 1990; Schiemann et al. 2009; Hudson 2012). In the boreal winter, the EAPJ and EASJ are strong and located along the southern and northern sides of the Tibetan Plateau (TP), respectively (see Fig. 1 in Luo and Zhang 2015). The two jets can induce not only circulation changes (Kug et al. 2010), but also significant temperature and precipitation changes over East Asia (Kuang

Corresponding authors: Dr. Danqing Huang, huangdq@nju.edu.cn; Prof. Aiguo Dai, adai@albany.edu

DOI: 10.1175/JCLI-D-18-0218.1

and Zhang 2005; Ren and Zhang 2007; Zhang et al. 2008; Huang et al. 2011). Thus, understanding recent changes in the two jets can help explain recent climate variations over East Asia, and it may also provide insights into how the two jets may respond to future climate changes.

In recent years, many studies have recognized the importance of the concurrent variations of the EAPJ and EASJ, rather than the variation of a single jet, since they reflect the interactions between the low- and high-latitude circulations over East Asia (Liao and Zhang 2013; Huang et al. 2014; Li and Zhang 2014; Huang et al. 2015; Zhu et al. 2016; Wang and Zhang 2015; Luo and Zhang 2015; D. Huang et al. 2017). For example, the concurring equatorward shift of the EAPJ and the poleward shift of the EASJ from 1985–98 to 1999–2013 are accompanied by a northwestward shift of the Siberian high and an enhanced northern East Asian trough, leading to cold winters in northern East Asia (Luo and Zhang 2015) and the abundant winter precipitation over northeastern China (D. Huang et al. 2017). An enhanced EASJ and a weakened EAPJ act as a bridge to bring the cold and warm air together, which results in persistent snowstorms in January 2008 over southern China (Liao and Zhang 2013).

Recently, D. Huang et al. (2017) showed that the winter EAPJ and EASJ shifted equatorward and poleward, respectively, during the warming hiatus period (Dai et al. 2015) from 1999 to 2013, compared with the rapid warming period from 1985 to 1998. These shifts are accompanied by a combination of a negative phase of the interdecadal Pacific oscillation (IPO; Power et al. 1999; Dai 2013; Dong and Dai 2015; Dong et al. 2018) and a positive phase of the Atlantic multidecadal oscillation [AMO; Enfield et al. 2001; Trenberth and Shea 2006; also referred to as the Atlantic multidecadal variability (AMV); Liu 2012]. The positive IPO is associated with warm sea surface temperatures (SSTs) in the central and eastern tropical Pacific and cold SSTs in the western and extratropical Pacific, while the positive AMO is associated with warm SSTs in the North Atlantic. The IPO and AMO are the most pronounced modes for decadal to multidecadal variations in SSTs and other related climate fields (Liu 2012), and they have large influences on the precipitation, temperature, and atmospheric circulations across the globe (Li et al. 2009; Mohino et al. 2011; Pui et al. 2011; Dai 2013; Dong and Dai 2015; Zhu et al. 2015; Si and Ding 2016; Fuentes-Franco et al. 2016; Lyu et al. 2017).

In fact, the concurrent variations of IPO and AMO have greater effects than their individual influences. For example, McCabe et al. (2004) found that the droughts with broad impacts (e.g., in 1996, 1999–2002) were mainly associated with the combination of a negative phase of the IPO (−IPO) and a positive phase of the AMO (+AMO). Atmospheric model simulations also show that the largest precipitation response over the United States occurs when the tropical Pacific and North Atlantic Oceans have SST anomalies of opposite signs that are associated with opposite phases of the IPO and AMO (Schubert et al. 2009). Mohino et al. (2011) examined the relative impact of the IPO and AMO on the Sahelian precipitation and revealed that the positive phase of the IPO (+IPO) leads to drought over the Sahel, while +AMO enhances the Sahelian rainfall. Joshi and Rai (2015) indicated that the opposite phases of IPO and AMO together modulated rainfalls over the western central and northeastern regions of India. These studies have emphasized the important role of the concurring opposite phases of the IPO and AMO for precipitation variations. However, little attention has been paid to their impacts on atmospheric circulations, particularly over East Asia. Meanwhile, we noticed that both the EAPJ and EASJ experienced significant changes in the late 1970s and late 1990s (Yu and Zhou 2007; Zhang and Huang 2011), such as the southward (Yu and Zhou 2007; Zhang and Huang 2011) and westward (Du et al. 2009) shifts of the EASJ around the late 1970s and the meridional shift of the EASJ and EAPJ since 1999 (D. Huang et al. 2017). It remains unclear whether there is any linkage between changes of the EAPJ and EASJ and the oceanic conditions over the Pacific and Atlantic associated with the IPO and AMO, respectively.

SST variations can induce changes in the two jets (Ren et al. 2008; Lu et al. 2013; Huang et al. 2014). On the one hand, the IPO- and AMO-induced SST changes may alter the meridional temperature gradients (MTG) in the troposphere (e.g., Seidel et al. 2008; Si et al. 2009; Yim et al. 2016) that affect the EAPJ and EASJ (D. Huang et al. 2017) via the thermal wind relation (Wallace and Hobbs 2005; Zhang and Huang 2011). On the other hand, both barotropic and baroclinic processes are important for variations in jet streams (Lee 2000). The background flow, thermal gradient, and eddy heat fluxes are closely related to the baroclinic eddy growth (Lee et al. 2011). The IPO- and AMO-induced SST changes may affect thermal conditions and impact the atmospheric baroclinicity in midlatitudes (Eady 1949; Xiao and Zhang 2015) and barotropic conditions in low latitudes (Lee et al. 2012; Kuang et al. 2014) and thus lead to the changes of the EAPJ and EASJ.

In this study, both the reanalysis data and atmospheric model simulations are analyzed to answer the following two questions:

1) How do the EAPJ and EASJ respond to the different phase combinations of the IPO and AMO?

2) What are the possible mechanisms for the IPO and AMO to cause variations in the EAPJ and EASJ?

The rest of the paper is organized as follows. Section 2 describes the data and method. The linkage between the EAPJ and EASJ variations and different combinations of the IPO and AMO is examined in section 3. In section 4, we propose a possible mechanism for the recent changes from 1979–98 to 1999–2014 in the two jets based on diagnostic analyses. Numerical experiments using an atmospheric general circulation model (AGCM) are also used to explore the relative contributions of the IPO and AMO in section 4. The summary and discussion are provided in section 5.

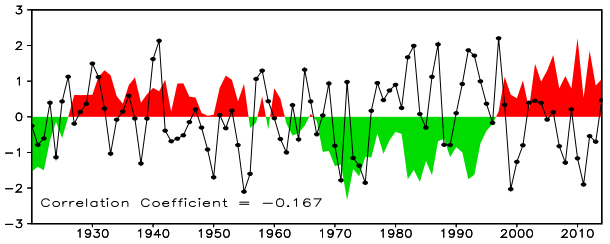

FIG. 1. Time series of the normalized DJF IPO (black line) and AMO (shading) indices during 1920–2014, derived as the PC of the second leading EOF of 3-yr-moving-average annual SSTs in near-global (60°S–60°N) oceans (for IPO) and PC1 of the EOF1 of the detrended annual SST over the North Atlantic (20°–70°N, 70°W–0° for AMO). The correlation coefficient between the two series is −0.167.

2. Data and method

a. Data

The datasets used in this study include the following products for the boreal winter [December–February (DJF)]:

1) Four reanalysis datasets for upper-air daily and monthly fields are used. These include the Twentieth Century Reanalysis version 2 from 1920 to 2014 on a 2° × 2° grid (20CR; Compo et al. 2011), the ECMWF interim reanalysis (ERA-Interim) from 1979 to 2014 on a 1° × 1° grid (Dee et al. 2011), the Modern-Era Retrospective Analysis for Research and Applications from 1979 to 2014 on a ~0.67° × 0.5° grid (MERRA 2; Gelaro et al. 2017), and the National Centers for Environmental Prediction–National Center for Atmospheric Research reanalysis from 1979 to 2014 on a 2.5° × 2.5° grid (NCEP–NCAR; Kalnay et al. 1996).
2) To force an atmospheric model and for quantifying the role of the IPO and AMO, we used the global monthly SST dataset on a 1° × 1° grid from 1870 to 2014 from the Hadley Centre Sea Ice and Sea Surface Temperature dataset (HadISST; Rayner et al. 2003), obtained from https://www.metoffice.gov.uk/hadobs/hadisst/data/download.html. To compare the DJF SST changes from 1979–98 to 1999–2014, we also used the global monthly SST dataset on a 2° × 2° grid from 1854 to 2014 from the National Oceanic and Atmospheric Administration (NOAA) Extended Reconstructed SST, version 5 (ERSSTv5; B. Huang et al. 2017), obtained from https://www.esrl.noaa.gov/psd/data/gridded/data.noaa.ersst.v5.html.
3) The IPO and AMO index data from 1920 to 2014 are derived as in Dai (2013), Dai et al. (2015), and Dong and Dai (2015). The IPO index is the principal component (PC) of the second leading empirical orthogonal function (EOF) of the 3-yr-moving-average annual SST fields over the globe from 60°S to 60°N, and the AMO index is the PC1 of the EOF1 of the linearly detrended annual SST over the North Atlantic (20°–70°N, 70°W–0°) domain from 1920 to 2014 (Fig. 1) based on HadISST. These EOF modes represent the IPO and AMO patterns mainly in the Pacific and North Atlantic Oceans, respectively (Dai et al. 2015). To examine the different phase combinations of the IPO and AMO during 1920–2014, 95 years of the index data were divided into four different groups depending on the normalized IPO and AMO phase combination, as shown in Fig. 2. A composite analysis was carried out to examine the atmospheric circulation anomalies (relative to the 1920–2014 mean) for each group by averaging over all the years within the group. For this purpose, we used the raw PC series for the IPO or AMO index without the decadal smoothing of the PC series that is often used for deriving a smoothed IPO or AMO index, as done previously (e.g., Dai 2013; Meehl et al. 2013; Dong and Dai 2015; Meehl et al. 2016). For comparison, the other three AMO indices from Enfield et al. (2001), Trenberth and Shea (2006), and Sutton and Dong (2012) have been examined.

b. Method

Following Ren et al. (2011), a jet core is identified if 1) the wind speed at 300 hPa is higher than 30 m s^{-1} for any given day and grid point, and 2) the wind speed at the central point is larger than that at its eight surrounding points within our analysis domain, which covers 20°–70°N, 65°–160°E. Here, the wind speed is the amplitude of the wind vector.

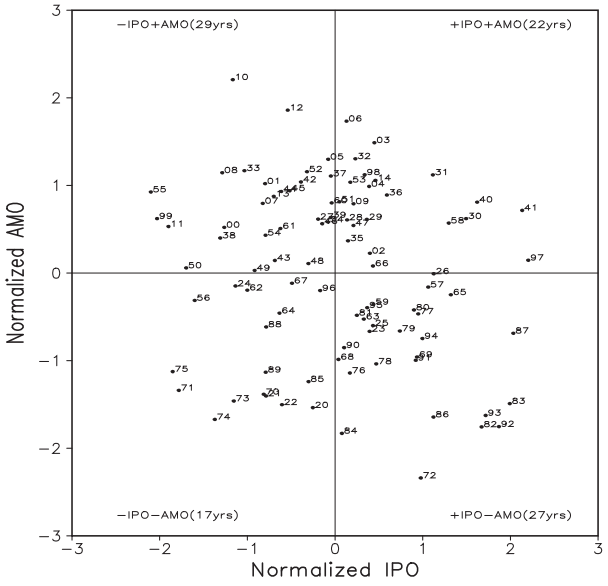

FIG. 2. Scatter diagram for the normalized DJF IPO index against the normalized winter AMO index during 1920–2014. The years 20–99 mean 1920–99, while the years 00–14 mean 2000–14. A negative (positive) phase of IPO is denoted as −IPO (+IPO), and similarly for AMO.

To select the key regions for the EAPJ and EASJ, the occurrence number of jet cores at each grid point over our analysis domain was calculated using the daily data from the four reanalysis datasets mentioned above. Following Luo and Zhang (2015) and D. Huang et al. (2017), the regions of 50°–60°N, 75°–90°E and 25°–32°N, 80°–120°E were chosen as the active regions of the EAPJ and EASJ, respectively, from the reanalysis datasets.

The MTG over a tropospheric layer is estimated as $\Delta\overline{T}/a\Delta\phi$, where $\Delta\overline{T}$ is the difference of the vertically averaged temperature from the surface to 300 hPa between two adjacent zonal bands with a latitude distance of $\Delta\phi$ (radians) within 20°–70°N, and a is Earth's radius.

The baroclinicity can be expressed in terms of the Eady growth rate σ, which is defined as (Eady 1949)

$$\sigma = 0.31\left(\frac{f}{N}\right)\left(\frac{dV}{dz}\right), \tag{1}$$

where f is the Coriolis parameter, N is the Brunt–Väisälä frequency, V is the time-mean horizontal wind velocity, and z is the vertical height. The value of σ averaged between 700 and 850 hPa is used in our study, since the baroclinic development primarily occurs in the lower troposphere (Lunkeit et al. 1998). Since the vertical shear is closely associated with the horizontal temperature gradient (Lehmann et al. 2014), a positive Eady growth rate would increase baroclinicity, often due to increased horizontal temperature gradients, and thus increase upper-level winds.

The anomalous meridional advection of heat and momentum would affect the large-amplitude stationary waves, which are generally accompanied by the jets (e.g., Klein 1983; Panetta 1993; DeWeaver and Nigam 2000; Wang et al. 2009; Xiao and Zhang 2012; Xue and Zhang 2017). Thus, we chose the meridional transport of zonal momentum $\overline{u'v'}$ and sensitive heat $\overline{T'v'}$ by synoptic eddies to study their impacts on the jets by the daily data (Kuang et al. 2014).

Changes in the interactions between the mean flow and transient eddies would transfer the available potential energy to the atmospheric time-mean flow and therefore impact the variation of the jets (e.g., Lee et al. 2012; Huang et al. 2014). The changes are quantified by analyzing barotropic and baroclinic energy conversions in the quasigeostrophic framework based on Cai et al. (2007). Following this framework, two energy conversions are calculated, including the barotropic energy conversion (BTEC) and the baroclinic energy conversion (BCEC), from mean available potential energy to eddy available potential energy. The BTEC can be expressed by the inner product of the **D** vector of the basic flow and the **E** vector of the transient parts (Cai et al. 2007):

$$\mathbf{D} = \left(\frac{\partial\overline{u}}{\partial x} - \frac{\partial\overline{v}}{\partial y}, \frac{\partial\overline{v}}{\partial x} + \frac{\partial\overline{u}}{\partial y}\right), \tag{2}$$

$$\mathbf{E} = \left[\frac{1}{2}\left(\overline{v'^2} - \overline{u'^2}\right), -\overline{u'v'}\right], \tag{3}$$

$$\mathrm{BTEC} = \frac{P_0}{g}\left[\frac{1}{2}\left(\overline{v'^2} - \overline{u'^2}\right)\left(\frac{\partial\overline{u}}{\partial x} - \frac{\partial\overline{v}}{\partial y}\right) + \left(-\overline{u'v'}\right)\left(\frac{\partial\overline{v}}{\partial x} + \frac{\partial\overline{u}}{\partial y}\right)\right]. \tag{4}$$

The BCEC is roughly proportional to the poleward eddy heat flux multiplied by the meridional temperature gradient (Cai et al. 2007):

$$C_1 = \left(\frac{P_o}{P}\right)^{C_v/C_p}\frac{R}{g}, \tag{5}$$

$$C_2 = C_1\left(\frac{P_0}{P}\right)^{R/C_p}\Big/\left(-\frac{d\theta}{dp}\right), \tag{6}$$

$$\mathrm{BCEC} = -C_2\left(\overline{u'T'}\frac{\partial\overline{T}}{\partial x} + \overline{v'T'}\frac{\partial\overline{T}}{\partial y}\right), \tag{7}$$

where g is the acceleration of gravity; P_o is 1000 hPa; R is the gas constant for dry air; c_p (c_v) is the specific heat of dry air at the constant pressure (volume); θ is the potential temperature; and u, v, and T are the zonal wind, meridional wind, and temperature at 300 hPa, respectively. The

overbar and prime represent the climatological mean and transient part, respectively. All the transient variables are 2–8-day variations derived using a bandpass filter and are on 300 hPa.

Regression and composite analyses are used in this study. The statistical significance of a difference or a regression coefficient is assessed using a Student's t test at the 90% confidence level.

The standard partial correlation (e.g., Saji and Yamagata 2003; Zhu et al. 2013) is also used to provide a lower bound of the independent contribution by the IPO or AMO to an atmospheric field. This method involves the correlation between two variables (say, x and y) while eliminating the influence of a third variable (say, z) by first removing all the variations associated with z from x and y. In our case, the IPO index is highly correlated with the AMO index during 1979–2014 (with a correlation coefficient $r = -0.53$). For example, to remove the influence from the AMO on an atmospheric variable (e.g., 300-hPa wind speed, denoted as the y variable), here we will consider the AMO index as the independent variable z and the IPO index as the predictor (x variable) for y and use the standard partial correlation coefficient

$$r_{xy,z} = \frac{r_{xy} - r_{xz}r_{yz}}{\sqrt{(1 - r_{xz}^2)}\sqrt{(1 - r_{yz}^2)}} \tag{8}$$

as a measure of the influence of the IPO on the atmospheric variable (i.e., 300-hPa wind speed) with the AMO's influence being removing through linear regression. Here, r_{ij} is the correlation between the variables i and j. The statistical significance of the correlation coefficient is assessed using a two-tailed t test at the 90% confidence level.

c. Model experiments

We used the CESM1.2.0 with the CAM5 physics (Neale et al. 2012) for the experiments (Table 1) that were forced by the observed monthly SSTs and sea ice concentrations from HadISST. We selected the finite-volume dynamical core configured with a horizontal resolution of 2.5° longitude × 1.9° latitude and 30 vertical hybrid levels. We used the default initial files for atmosphere and land conditions at the year-2000 level, which were provided by CESM1.2.0. All the simulations were integrated for 31 years, with the last 30 years being used in our analyses.

In the CTRL run, the climatological monthly SST averaged from 1979 to 2014 was used. Five sensitivity experiments—EXP_All, EXP_P, EXP_A, EXP_AP, and EXP_IP—are similar to CTRL but with monthly SST anomalies, which are the 1999–2014 minus 1979–98 mean difference based on HadISST, added to the climatological monthly SST over the globe, the Pacific, the North Atlantic, both the Pacific and North Atlantic, and both the Indian and Pacific Oceans, respectively. These ocean domains are shown in Fig. 3, together with the SST anomalies for January. The experiment EXP_All can be used to quantify the model's ability to simulate the recent jet shifts, as the circulation differences between EXP_All and CTRL may be compared with those between 1999–2014 and 1979–98 in the reanalysis. We realize that these SST differences include not only the SST anomalies induced by the IPO and AMO, but also the changes caused by the recent external forcing (Trenberth and Fasullo 2013; Zhang 2016), although the IPO-related SST change pattern seems to dominate in the Pacific (Fig. 3). Here, we used these simple decadal differences to qualitatively represent the SST forcing associated with the IPO and AMO, while the Indian SST difference reflects the recent changes in the oceanic conditions in that basin. It should be emphasized that the EXP_P and EXP_A experiments only attempt to simulate the influence directly coming from the Pacific IPO-related or Atlantic AMO-related SST forcing. In the real world, it is possible that the other ocean basins may respond to the IPO- or AMO-related SST forcing and thus further impact East Asian jets. These additional impacts are partially included in the EXP_AP and EXP_IP experiments. Because of this, we expect the response in the EXP_P and EXP_A experiments to be on the lower end of the impact from the IPO or AMO, as seen in the real world.

TABLE 1. Atmospheric model experiments carried out in this study.

Experiment name	SST configuration
CTRL	Climatological (monthly) SST averaged from 1979 to 2014
EXP_All	Climatological SST + SST anomalies[a] over the globe
EXP_P	Climatological SST + SST anomalies over the Pacific Ocean
EXP_A	Climatological SST + SST anomalies over the North Atlantic
EXP_AP	Climatological SST + SST anomalies over both the Pacific and North Atlantic Oceans
EXP_IP	Climatological SST + SST anomalies over both the Indian and Pacific Oceans

[a] The SST anomalies are the monthly mean SST differences between 1999–2014 and 1979–98 based on HadISST.

3. EAPJ and EASJ variations and the IPO and AMO phase combinations

For each of the four IPO and AMO phase combinations (Fig. 2), we estimated the composite mean of 300-hPa wind speed (Figs. 4a–d) as the mean wind speed

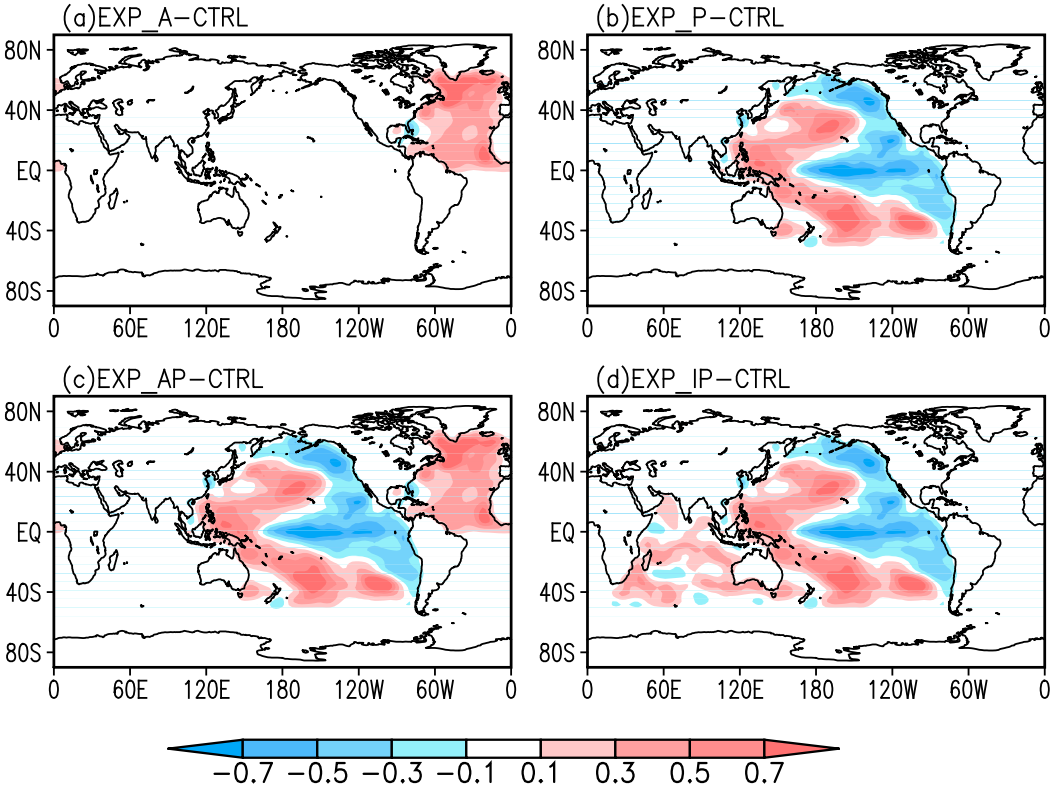

FIG. 3. Mean SST anomalies (°C) for January added to the long-term (1979–2014) SST climatology for (a) EXP_A, (b) EXP_P, (c) EXP_AP, and (d) EXP_IP. They were derived as the monthly mean SST differences between 1999–2014 and 1979–98 based on HadISST.

averaged over all the years within a given group. These composite wind speeds are characterized by zonally prolonged EASJ along 30°N, while it is difficult to examine the patterns of the EAPJ in Figs. 4a–d, as its intensity is much weaker than that of the EASJ. The differences among the four composite wind speeds are shown more clearly by wind velocity anomalies (relative to the 1920–2014 mean) in Figs. 4e–h. In the "+IPO +AMO" (Fig. 4e) and "−IPO −AMO" groups (Fig. 4g), there are no significant wind speed anomalies in the active regions of the two jets. However, in the "+IPO −AMO" (Fig. 4f) and the "−IPO +AMO" groups (Fig. 4h), a tripole anomaly pattern is evident along the active regions of the two jets, with positive anomalies between them and negative anomalies to the south of the EASJ and north of the EAPJ for the −IPO +AMO group (Fig. 4h) and roughly the opposite for the +IPO −AMO group (Fig. 4f). This pattern is particularly evident in the difference between the −IPO +AMO and +IPO −AMO groups (Fig. 5a) and is more obvious during 1979–2014 (Fig. 5c) than 1920–78 (Fig. 5b). We further tested the sensitivity of our results to different definitions of the AMO index. Using the three other AMO indices from Enfield et al. (2001), Trenberth and Shea (2006), and Sutton and Dong (2012), the composite 300-hPa wind speed anomalies were examined in the four phase groups (figure not shown). Similar results were found with a tripole anomaly pattern along the active regions of the two jets in the +IPO −AMO and the −IPO +AMO groups.

In fact, opposite phases of the IPO and AMO have occurred for most years during 1979–2014, with the +IPO −AMO group seen mostly during 1979–98 and the −IPO +AMO group mostly during 1999–2014 (Fig. 1). The SST changes from 1979–98 to 1999–2014 are shown in Fig. 6 based on the HadISST and ERSSTv5 datasets. They show similar SST changes that resemble those associated with the negative phase of the IPO over the Pacific (e.g., Power et al. 1999; Dai 2013; Dong and Dai 2015). Substantial warming also exists over the Atlantic Ocean (Fig. 6), and it resembles the positive phase of the AMO (e.g., Enfield et al. 2001; Knight et al. 2006; Dai et al. 2015). Thus, there may exist a linkage between opposite phases of the IPO and AMO and variations of the two jets during 1979–2014.

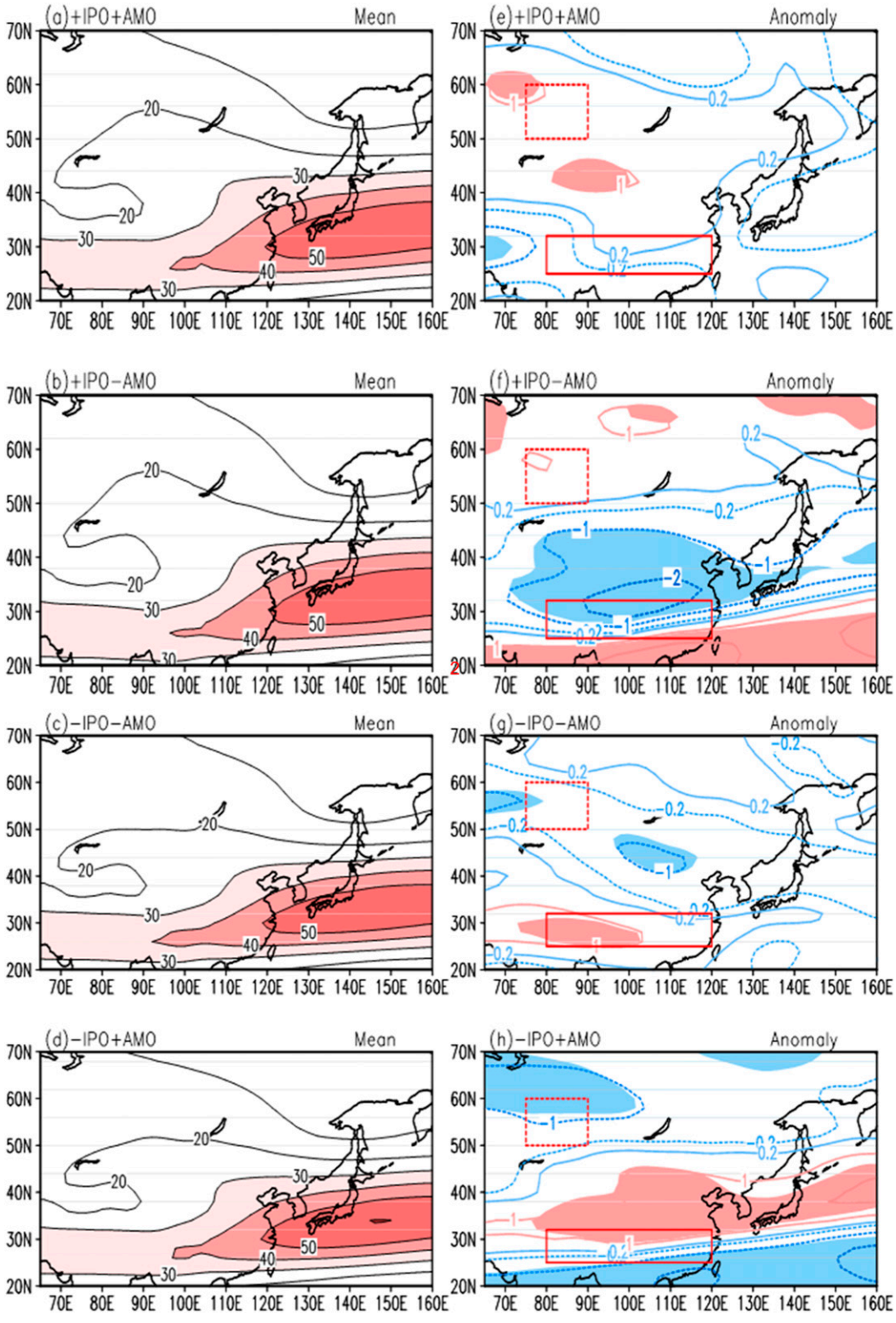

FIG. 4. (a)–(d) The 300-hPa DJF composite-mean wind speed ($m\,s^{-1}$) and (e)–(h) anomalies relative to the 1920–2014 mean ($m\,s^{-1}$) for (a),(e) +IPO +AMO, (b),(f) +IPO −AMO, (c),(g) −IPO −AMO, and (d),(h) −IPO +AMO based on the 20CR. The years of each group are shown in Fig. 2. The values above 30 $m\,s^{-1}$ are shaded in (a)–(d). The red dashed (solid) box in (e)–(h) indicates the active region of the EAPJ covering 50°–60°N, 75°–90°E (EASJ covering 25°–32°N, 80°–120°E). The color shadings in (e)–(h) indicate that the differences are significant at the 90% level based on a Student's *t* test.

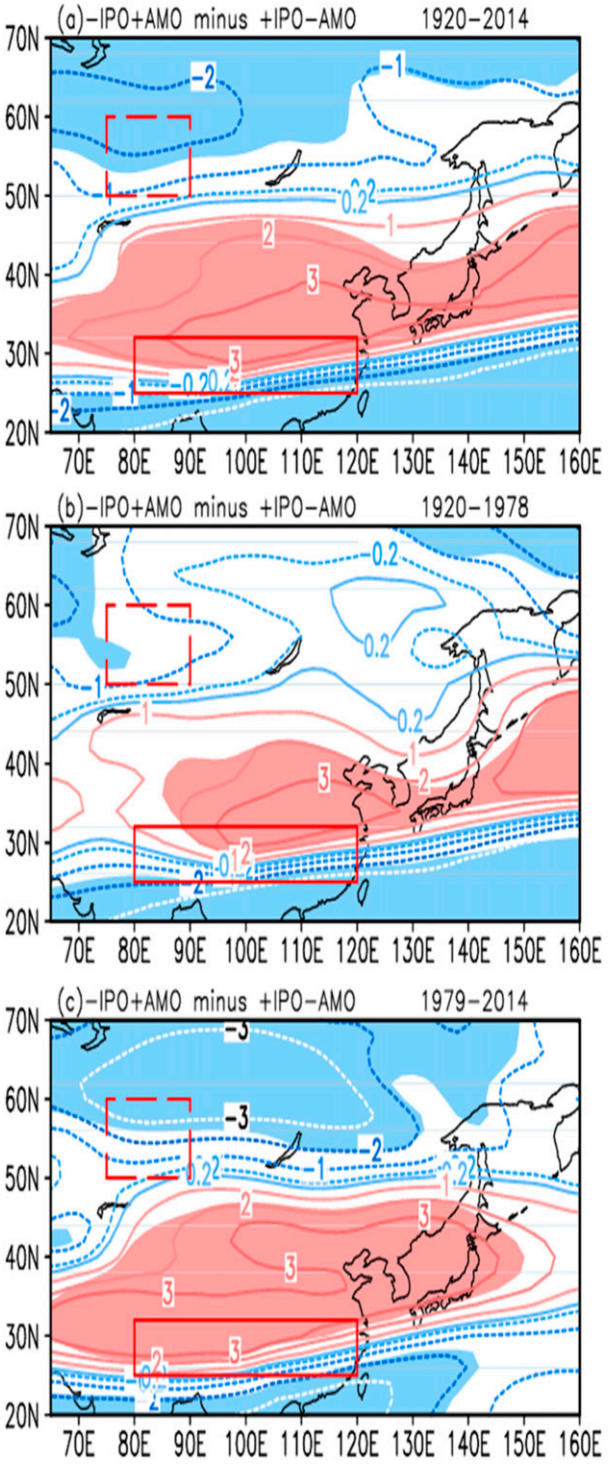

FIG. 5. The 300-hPa DJF composite-mean wind speed differences (m s^{-1}) between −IPO +AMO and +IPO −AMO based on the 20CR during (a) 1920–2014, (b) 1920–78, and (c) 1979–2014. The duration of each group is shown in Fig. 2. The red dashed (solid) box indicates the active region of the EAPJ (EASJ). The color shading indicates that the differences are significant at the 90% level based on a Student's *t* test.

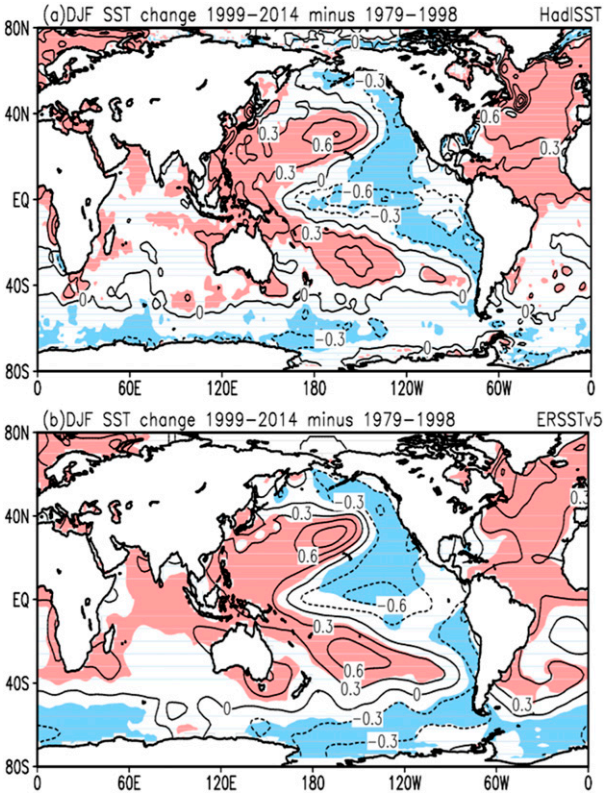

FIG. 6. DJF SST differences (°C) between 1999–2014 and 1979–98 from the (a) HadISST and (b) ERSSTv5. The shading indicates that the difference is significant at the 90% level based on a Student's *t* test.

We further examined the difference between 1999–2014 and 1979–98 in 300-hPa wind speed from four reanalysis products in Fig. 7, which shows a clear tripole anomaly pattern along the EAPJ and EASJ. This pattern resembles the wind speed differences for the −IPO +AMO minus +IPO −AMO groups during 1979–2014 (Fig. 5c), which is expected, given that the −IPO +AMO and +IPO −AMO years are mainly within 1999–2014 and 1979–98, respectively (Fig. 2). Since the ERA-Interim has good performance in quantifying atmospheric circulations over East Asia (Huang et al. 2016; Zhu et al. 2017), in the following, we will discuss the results based on the ERA-Interim only and focus on atmospheric circulation differences between 1999–2014 and 1979–98, which largely represent the −IPO +AMO and +IPO −AMO groups, respectively.

4. Mechanisms for the recent EAPJ and EASJ variations

a. Diagnostic analysis

To understand possible mechanisms for jet changes between 1999–2014 and 1979–98, the MTG and Eady

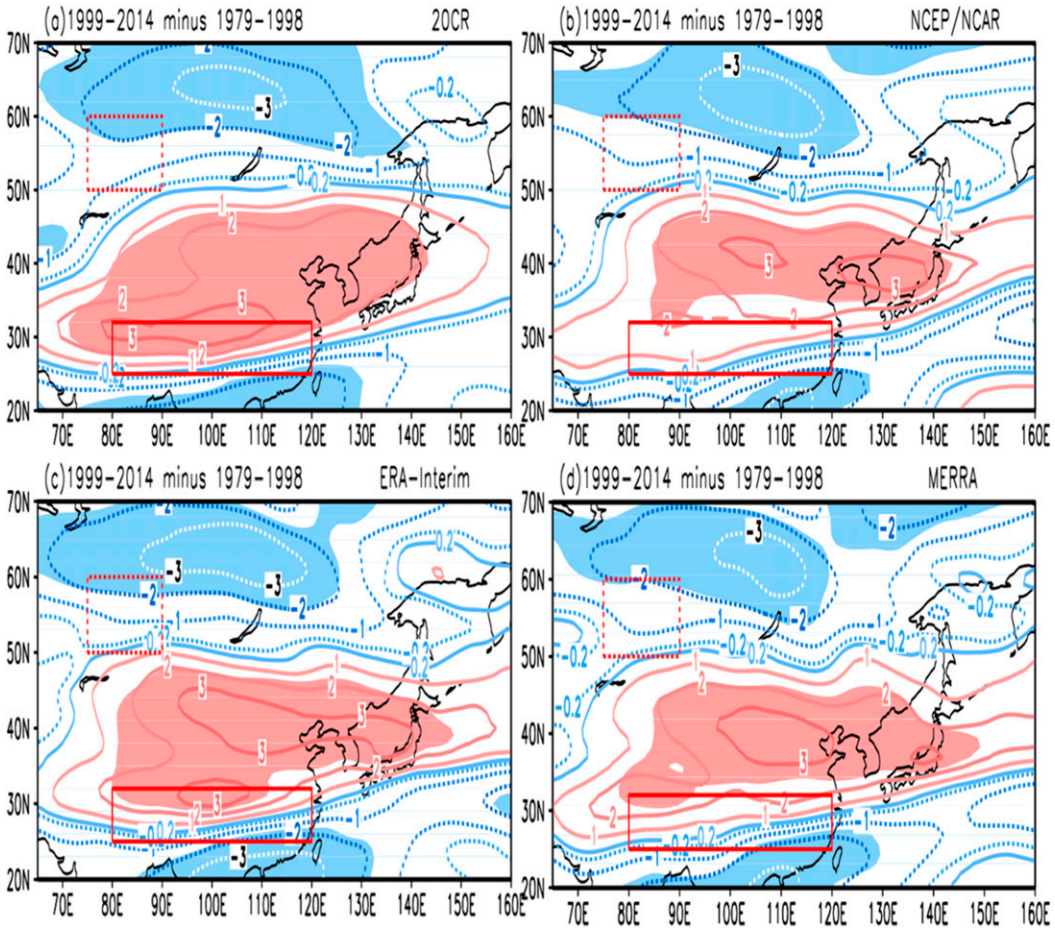

FIG. 7. The 300-hPa DJF wind speed differences between 1999–2014 and 1979–98 ($m\,s^{-1}$) from the (a) 20CR, (b) NCEP–NCAR, (c) ERA-Interim, and (d) MERRA. The red dashed (solid) box indicates the active region of the EAPJ (EASJ). The shading indicates that the difference is significant at the 90% level based on a Student's *t* test.

growth rate σ differences are shown in Fig. 8. Since the climatological MTG is negative over the Northern Hemisphere as air temperature decreases from the equator to the North Pole, a negative (positive) MTG anomaly should intensify (weaken) the background MTG. A tripole temperature anomaly pattern is seen over the two jet regions (Fig. 8a) that can alter the background westerlies through the thermal wind relationship. The negative MTG anomaly over 30°–50°N should intensify the MTG and thus strengthen the westerlies there, while the positive MTG anomalies to the south and north of this region would weaken the westerlies there. The positive–negative–positive MTG changes are consistent with the reduced–increased–reduced 300-hPa wind speed change patterns (figure not shown). The σ differences also show some positive anomalies over 30°–50°N and negative anomalies over the lower and higher latitudes (Fig. 8b). The positive σ anomalies are associated with increased horizontal temperature gradients and thus stronger westerlies over 30°–50°N. Meanwhile, the negative σ anomalies should weaken the westerlies over the lower and higher latitudes.

To analyze the relationship with the IPO and AMO, the patterns of the 300-hPa wind speed regressed against the unsmoothed IPO or AMO index (directly from Fig. 1) during 1979–2014 are shown in Fig. 9. Associated with the negative phase of IPO (and from ENSO), there is an alternating anomaly pattern in 300-hPa wind speed with strengthened winds around 30°–47.5°N and weakened winds to the north and south of it (Fig. 9a). This pattern is also evident for the positive phase of AMO, especially for the two anomalies over 30°–47.5°N and the high latitudes (Fig. 9b). This alternating anomaly pattern would lead to an equatorward shift of the EAPJ and a poleward shift of the EASJ, as winds strengthen equatorward around the EAPJ box but poleward around the EASJ box.

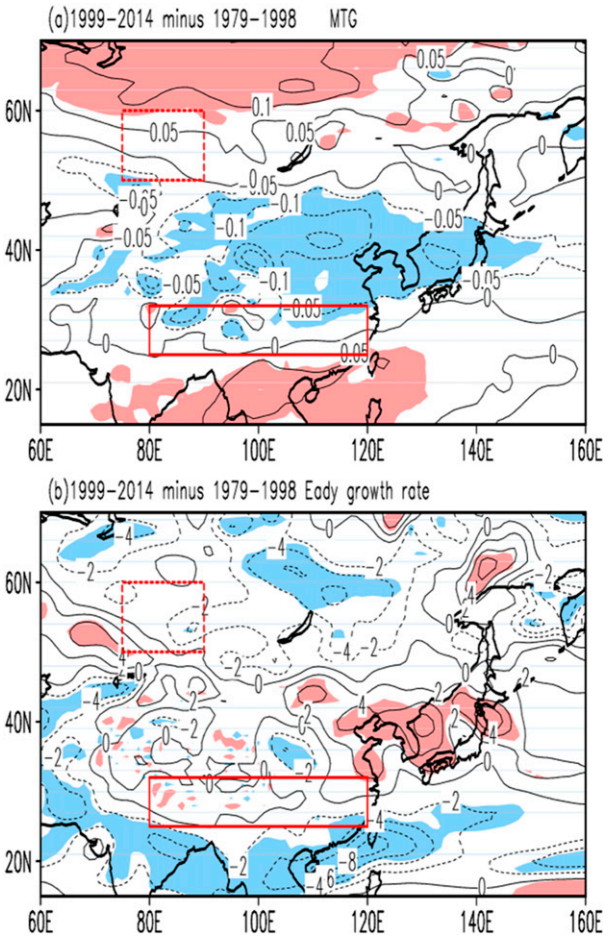

FIG. 8. The 1999–2014 minus 1979–98 difference of (a) DJF mean MTG (10^{-5} K m^{-1}) averaged from the surface to 300 hPa and the (b) Eady growth rate σ (day^{-1}). The red dashed (solid) box indicates the active region of the EAPJ (EASJ). The shading indicates that the difference is significant at the 90% level based on a Student's t test.

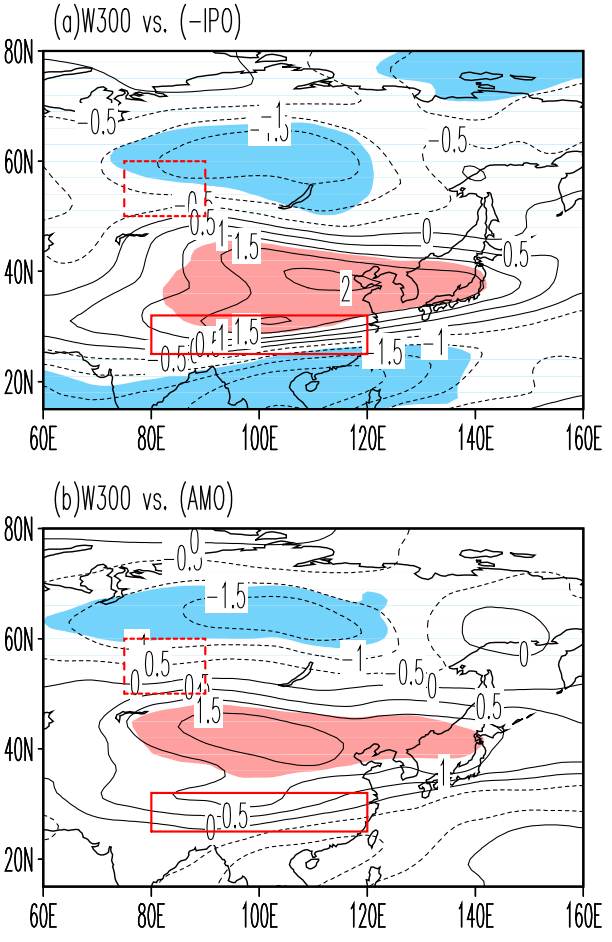

FIG. 9. Regression coefficients of DJF wind speed at 300 hPa against the (a) unsmoothed IPO index (multiplied by −1, indicating the negative phase of IPO; m s^{-1} per unit index) and (b) unsmoothed AMO index (m s^{-1} per unit index) during 1979–2014. The red dashed (solid) box indicates the active region of the EAPJ (EASJ). The shading indicates that the regression coefficient is significant at the 90% level based on a Student's t test.

To understand 300-hPa wind speed variations shown in Fig. 9, patterns of regressed MTG and σ against the unsmoothed IPO or AMO index are shown in Fig. 10. Associated with a negative IPO (Fig. 10a) and a positive AMO index (Fig. 10c), the negative MTG anomaly over 30°–50°N would intensify the background MTG and thus strengthen the westerlies there via the thermal wind relation. Meanwhile, the positive MTG anomalies over the higher and lower latitudes would weaken the westerlies there. Figures 10b and 10d show the regression patterns of mean σ against the unsmoothed IPO and AMO indices separately. Associated with a negative IPO, negative σ anomalies are located over the EAPJ region (Fig. 10b), while the positive σ anomalies are seen over the regions along 40°N associated with a positive AMO index (Fig. 10d), which should intensify the westerlies there due to the associated increase in horizontal temperature gradients. These results indicate that the decadal MTG and σ changes between the two periods are linked to the recent changes in the IPO and AMO phases and that the IPO- and AMO-induced MTG and σ can help explain the changes in the wind fields and the shifts of the two jets.

We realize that the IPO and AMO indices shown in Fig. 1 are highly correlated with $r = -0.53$ during 1979–2014. Thus, the regressed results against the IPO (Figs. 9, 10) may include the impact of the AMO, and vice versa. We used the partial correlation (Fig. 11) to further quantify the impacts of the IPO and AMO on the recent shifts of the two jets. The partial correlation

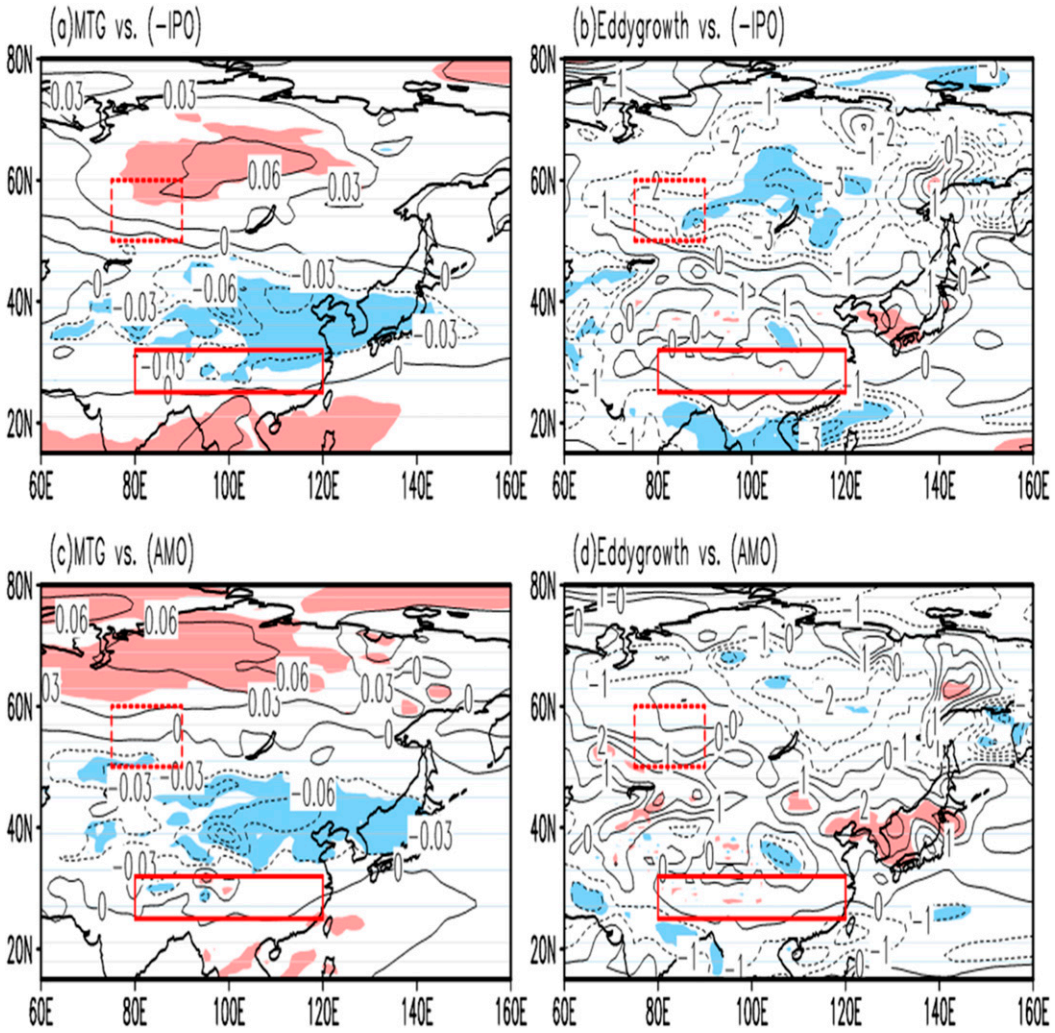

FIG. 10. As in Fig. 9, but for the (a),(c) regression coefficients of DJF MTG (10^{-5} K m^{-1} per unit index) and (b),(d) σ (day^{-1} per unit index) against the unsmoothed (a),(b) IPO index (multiplied by −1, indicating the negative phase of IPO) and (c),(d) AMO index during 1979–2014.

patterns with 300-hPa wind speed broadly resemble the regression patterns shown in Fig. 9, although the negative anomaly pattern south of the EASJ is less evident in Fig. 11b than in Fig. 9b. Figure 11 also suggests that the IPO plays a bigger role than the AMO for the recent 300-hPa wind changes and that a combination of the −IPO and +AMO may favor the recent jet shifts more than the individual ones. Thus, it is necessary to use model simulations to further investigate the mechanisms and relative contributions of a negative IPO and a positive AMO to the jet changes.

b. *Model results*

We first selected the active regions for the EAPJ and EASJ in the CTRL run. Figure 12a shows the occurrence number of jet cores at each grid point in the boreal winter based on the daily data from the CTRL run. The active regions of the EAPJ and EASJ are located over 50°–60°N, 65°–80°E (red dashed box in Fig. 12a) and the southern flank of the TP (25°–32°N, 65°–110°E; red solid box in Fig. 12a), respectively. Although these active regions are not exactly the same as those in the reanalysis data (Fig. 1 in Luo and Zhang 2015), the latitude zones are similar. Furthermore, the 300-hPa DJF climatological wind speed from the CTRL run (Fig. 12b) is also consistent with that from the reanalysis data (Fig. 2 in Huang et al. 2015), which show a center of strong winds over the latitude zone around 30°N, particularly over the ocean southeast of Japan. Thus, the model can generally capture latitude bands of the two jets.

We then examined the model's ability to simulate the recent shifts of the EAPJ and EASJ. The 300-hPa wind

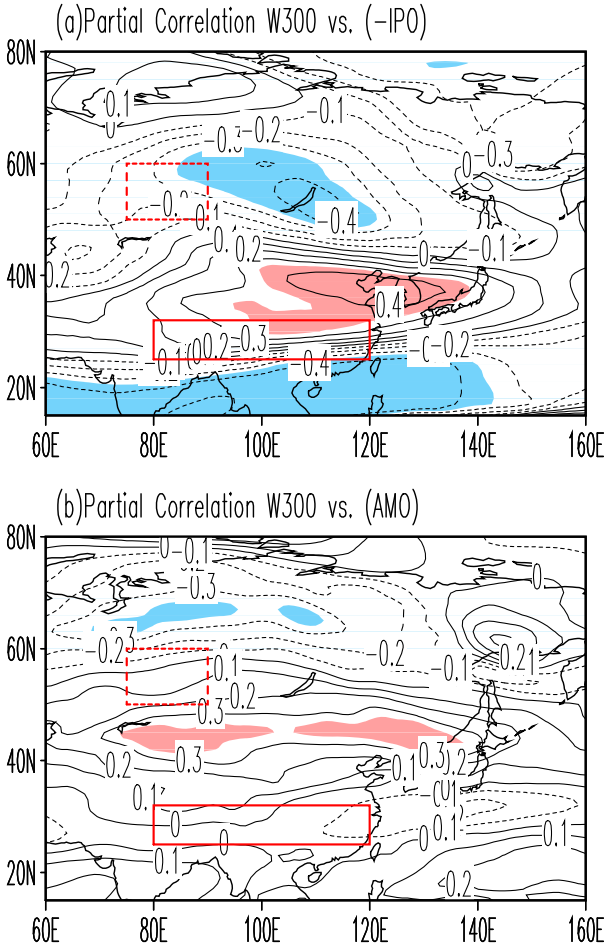

FIG. 11. Maps of partial correlation coefficients between the DJF wind speed at 300 hPa and the unsmoothed (a) IPO index (multiplied by −1, indicating the negative phase of IPO) and (b) AMO index. The red dashed (solid) box indicates the active region of the EAPJ (EASJ). The shading indicates that the regression coefficient is significant at the 90% level based on a two-tailed t test.

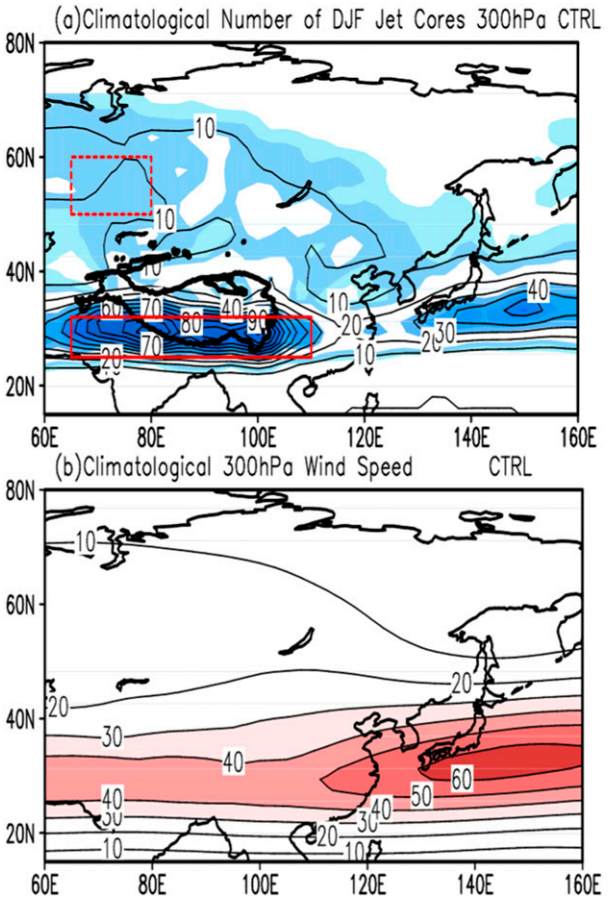

FIG. 12. (a) Climatological number of DJF jet cores at 300 hPa (days) and (b) the 300-hPa DJF climatological (last 30-yr mean) wind speed (m s^{-1}) in the CTRL run. Values above 24 in (a) are shaded in blue. The red dashed (solid) box in (a) indicates the active region of the EAPJ covering 50°–60°N, 65°–80°E (EASJ covering 25°–32°N, 65°–110°E). The thick black solid contour in (a) indicates the boundary of the TP. The values above 40 m s^{-1} are shaded in (b).

speed differences between the EXP_All and CTRL runs are shown in Fig. 13a. The EXP_All displays a tripole anomaly pattern with strengthened winds around 30°–50°N and weakened winds to the south and north of it. This anomaly pattern is qualitatively consistent with the differences between 1999–2014 and 1979–98 from ERA-Interim for the average over the East Asia sector (Fig. 13b), although the difference from the simulation is smaller than that from the reanalysis. Note the slightly different longitudes used for the averages in Fig. 13b, as the active regions of the two jets are different between the model and ERA-Interim. Thus, the model has the ability to qualitatively simulate the meridional shift of the EAPJ and EASJ and thus may be used to investigate the mechanisms of the recent meridional shifts of the jets.

We further analyzed the wind speed differences between the other four sensitive experiments and the CTRL run (Fig. 14). EXP_A displays an enhanced EAPJ and reduced EASJ (Fig. 14a), while EXP_P produces no significant changes in the EAPJ and EASJ regions (Fig. 14b). The EXP_AP experiment combines the SST forcing in the North Atlantic and the Pacific (Fig. 3), and it shows an alternating anomaly pattern in 300-hPa wind speed with strengthened winds around 35°–47.5°N and weakened winds to the south of it (Fig. 14c). This is qualitatively consistent with the differences between 1999–2014 and 1979–98 from the reanalysis data (Fig. 7). Since Indian Ocean SSTs have varied with the IPO (Li et al. 2015; Dong et al. 2016), the EXP_IP experiment is set up to quantify the combined role of the Indian Ocean and the IPO. As shown in

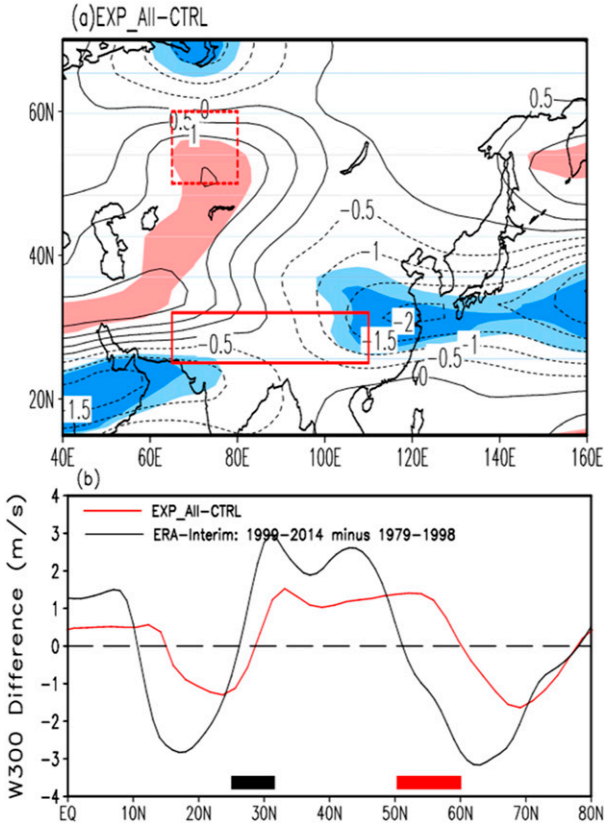

FIG. 13. (a) The 300-hPa DJF wind speed differences ($m\,s^{-1}$) between EXP_All and CTRL and (b) the 65°–80°E-mean 300-hPa DJF wind speed differences ($m\,s^{-1}$) between EXP_All and CTRL (red line) and 70°–100°E-mean 300-hPa DJF wind speed differences between 1999–2014 and 1979–98 from ERA-Interim (black line). The red dashed (solid) box in (a) indicates the active region of the EAPJ (EASJ). The pink and light blue (dark blue) shadings in (a) indicate that the difference is significant at the 90% (95%) level based on a Student's *t* test. The black and red boxes in (b) indicate the active latitude region of the EASJ and EAPJ, respectively.

Fig. 14d, EXP_IP can capture the strengthened winds at 300 hPa around 25°–40°N and weakened winds to the south of it. Although the significant anomalies expand farther to the west and the south, the latitudinal zones are near the maximum wind anomaly between EXP_AP and CTRL. Thus, the combined SST changes in the Indian and Pacific Oceans seem to play a bigger role in the recent changes of the two jets than the IPO alone.

The vertically averaged MTG differences from the model runs (Fig. 15) also support the simulated wind differences. For the EXP_A experiment (Fig. 15a), significant negative (positive) MTG anomalies over the EAPJ (EASJ) region would intensify (reduce) the background MTG and thus strengthen (weaken) the EAPJ and EASJ there via the thermal wind relation. This is consistent with the wind differences for the EXP_A experiment (Fig. 14a). Significant MTG differences for the EXP_P experiment (Fig. 15b) are seen over the western Pacific and thus affect the westerly winds there. Compared to the CTRL run, the EXP_AP experiment (Fig. 15c) shows negative MTG anomalies over the region of 35°–45°N. This should intensify the MTG and thus strengthen the westerlies there via the thermal wind relation (Fig. 14c). Meanwhile, the positive MTG differences over low latitudes should weaken the westerlies there. The negative MTG anomalies are also evident in EXP_IP (Fig. 15d), although the anomalies move southward to 30°–40°N, and it resembles that in EXP_AP (Fig. 15c) but differs from the MTG change in EXP_P (Fig. 15b).

Figure 16 shows the Eady growth rate σ differences between the sensitive experiments and the CTRL run. In the EXP_A experiment (Fig. 16a), a zonal positive σ anomaly is seen over the latitudes near 50°N, which should strength the westerly winds there, including the EAPJ. Consistent with the MTG differences for the EXP_P experiment (Fig. 15b), robust σ differences are also seen over the western Pacific, showing positive anomalies south of ~45°N and negative anomalies to the north and southwest of it in the EXP_P experiment (Fig. 16b). For the EXP_AP experiment, the positive σ anomaly over 35°–45°N should intensify the westerlies there due to the associated increases in horizontal temperature gradients, while the negative σ differences over the higher and lower latitudes should weaken the westerlies there (Fig. 16c). The MTG and σ differences are consistent with the wind differences between EXP_AP and CTRL. For the EXP_IP experiment (Fig. 16d), the positive σ differences are insignificant over the region of 35°–45°N, while negative σ differences over the higher and lower latitudes are seen (Fig. 16d), although the significant regions are smaller than those for EXP_AP (Fig. 16c). These results imply that the combined effects of a negative IPO and a positive AMO can lead to an equatorward shift of the EAPJ and a poleward shift of the EASJ in the boreal winter.

In the following, we used the EXP_AP experiment to further understand the possible mechanisms from the perspective of transient eddy variations and the energy conversion. Figure 17 shows the 65°–80°E (the longitudinal range of the activity regions of the EAPJ and EASJ) mean meridional eddy transport of zonal momentum $\overline{u'v'}$ and sensible heat $\overline{T'v'}$ in EXP_AP, CTRL, and the differences between them. The eddy transport of zonal momentum exhibits a single peak around 40°N in both EXP_AP and CTRL, but it is enhanced in EXP_AP along 35°–45°N (Fig. 17a). This could

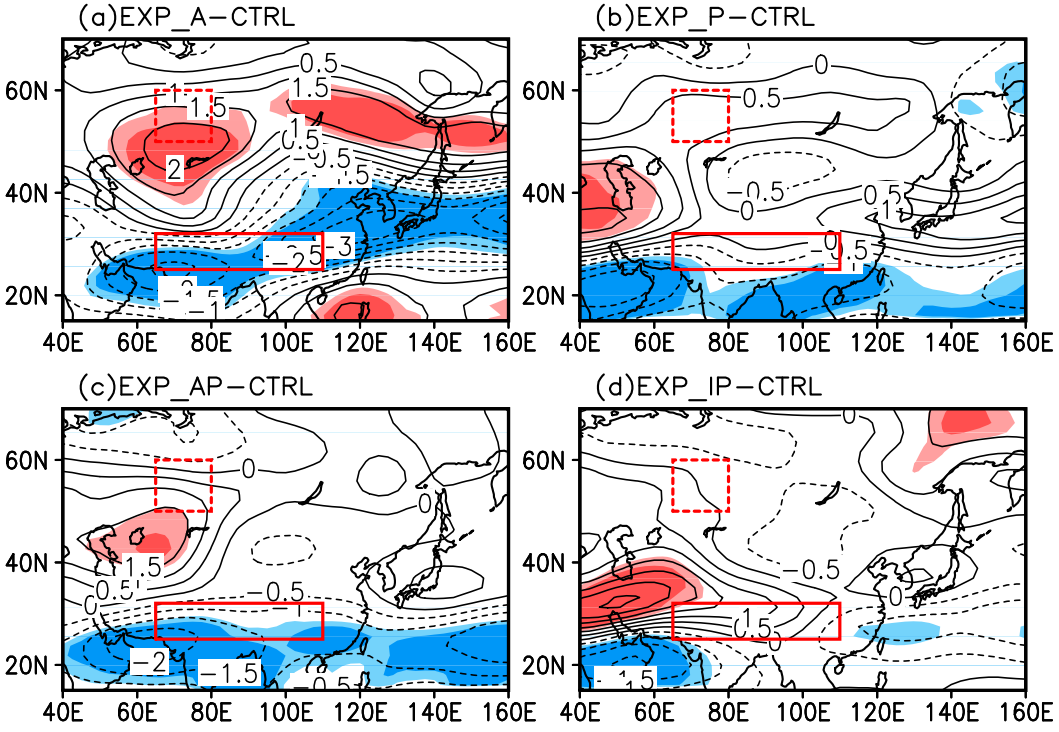

FIG. 14. The 300-hPa DJF wind speed differences ($m\,s^{-1}$) between (a) EXP_A and CTRL, (b) EXP_P and CTRL, (c) EXP_AP and CTRL, and (d) EXP_IP and CTRL. The red dashed (solid) box indicates the active region of the EAPJ (EASJ). The light (dark) shading indicates that the difference is significant at the 90% (95%) level based on a Student's *t* test.

strengthen the westerlies over there (Kuang et al. 2014). The meridional eddy transport of sensible heat shows double peaks around 28°–29° and 52°N (Fig. 17b), which are in the active regions of the EASJ and EAPJ, respectively. For the eddy heat transport, a positive anomaly over the midlatitude regions along 35°–45°N in the EXP_AP experiment (Fig. 17b) could enhance the westerlies there (Kuang et al. 2014).

Since the barotropic and baroclinic energy conversions can affect the transient eddies and mean flow and therefore results in the variation of the two jets (Lee 2000; Lee et al. 2012), we further examined them in the EXP_AP experiment. The EXP_AP minus CTRL difference of the 300-hPa barotropic energy conversion from the time-mean flow to eddies (Fig. 18a) shows some positive values over the active regions of the EAPJ and EASJ. This suggests that eddies gained more kinetic energy there, and the mean flow slowed down more in EXP_AP than in CTRL. However, the regions with significant values in Fig. 18a are smaller than those of the wind difference shown in Fig. 14c.

Differential heating of the atmosphere can affect the movement of air and provide the energy source for baroclinic wave development (Chang and Fu 2002) and therefore alter the jets (Lee et al. 2012). Figure 18b shows the EXP_AP minus CTRL difference of the baroclinic energy conversion from mean available potential energy to eddy available potential energy. Compared to the CTRL run, the baroclinic energy conversion has increased over the regions along 35°–45°N in EXP_AP. In particular, the pattern of increase is comparable to that of the wind speed difference (Fig. 14c). Lee et al. (2012) suggested that an advection contributes to increased baroclinicity that modulates the growth of baroclinic waves in the North Atlantic. As mentioned, this mechanism may also be used to explain the intensification of the westerlies over East Asia. In particular, due to the consistency of the significant positive BCEC anomaly (Fig. 18b) and the enhanced wind speed anomaly (Fig. 14c), the baroclinic energy conversion has contributed more than the barotropic energy conversion to the shifts of the EAPJ and EASJ associated with the negative IPO and positive AMO.

5. Conclusions and discussion

In this study, we have examined four different phase combinations of the AMO and IPO for their impacts on the winter EAPJ and EASJ. The response of the EAPJ and EASJ is significant in the −IPO +AMO and

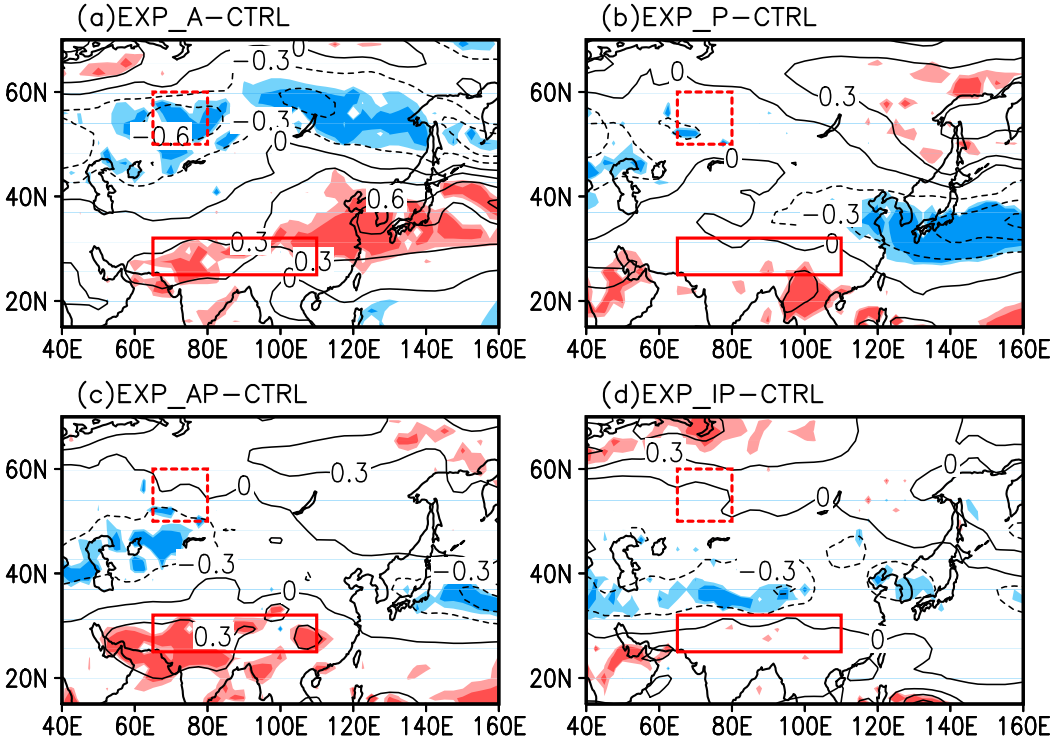

FIG. 15. As in Fig. 14, but for the DJF MTG differences (10^{-5} K m^{-1}) averaged from the surface to 300 hPa.

+IPO −AMO groups. A broad tripole anomaly pattern is seen along the active regions of EAPJ and EASJ, with positive anomalies between them and negative anomalies to the south and north of them for the −IPO +AMO group and the opposite in the +IPO −AMO group. This pattern is particularly evident in the jet differences between 1999–2014 (−IPO +AMO) and 1979–98 (+IPO −AMO). The IPO- and AMO-associated SST anomalies since 1999 have enhanced the tropospheric meridional temperature gradient (MTG) and Eady growth rate σ and thus westerlies over the region between the two jets, but weakened them to the south and north of the region, thereby contributing to the equatorward and poleward shifts, respectively, by the EAPJ and EASJ via the thermal relation and the increased horizontal temperature gradients. Partial correlations suggest that a combination of the −IPO and +AMO may favor the recent jet shifts more than the individual ones.

Five CESM1.2.0 (CAM5 based) model experiments forced by different combinations of the SST anomalies of 1999–2014 (relative to 1979–98) were carried out and analyzed to further examine the processes behind the recent jet changes in response to the −IPO +AMO-like SST anomalies from 1979–98 to 1999–2014. The model results suggest that without the SST response in other ocean basins, a negative phase of the IPO in the Pacific can only affect the 300-hPa wind speed over the ocean southeast of Japan, which may alter the oceanic EASJ, while a positive phase of the AMO in the Atlantic can only enhance the EAPJ and weaken the EASJ. The combined effects of the warming over the Indian Ocean and the negative phase of the IPO can enhance the wind speed between the EAPJ and EASJ, but the largest anomalies expand farther to the west. A combination of a negative-phase IPO and a positive-phase AMO, which resembles the recent decadal SST change, can lead to an equatorward and poleward shift of the EAPJ and EASJ, respectively, in the model, as seen in the reanalysis data. The model simulation also shows enhanced MTG and σ over the regions between the two jets, which would result in the shifts of the jets.

We further examined the synoptic-scale transient eddy activities in the model experiment forced with the −IPO +AMO-like SST anomalies. It is found that the meridional eddy transports of zonal momentum and sensitive heat strengthen over the regions between the two jets and enhance westerlies there due to the feedback between the stationary and transient synoptic eddies. The barotropic and baroclinic energy conversions in response to the −IPO +AMO-like SST forcing also contribute to the shifts of the two jets, particularly the baroclinic energy conversion from mean available potential energy to eddy available potential energy.

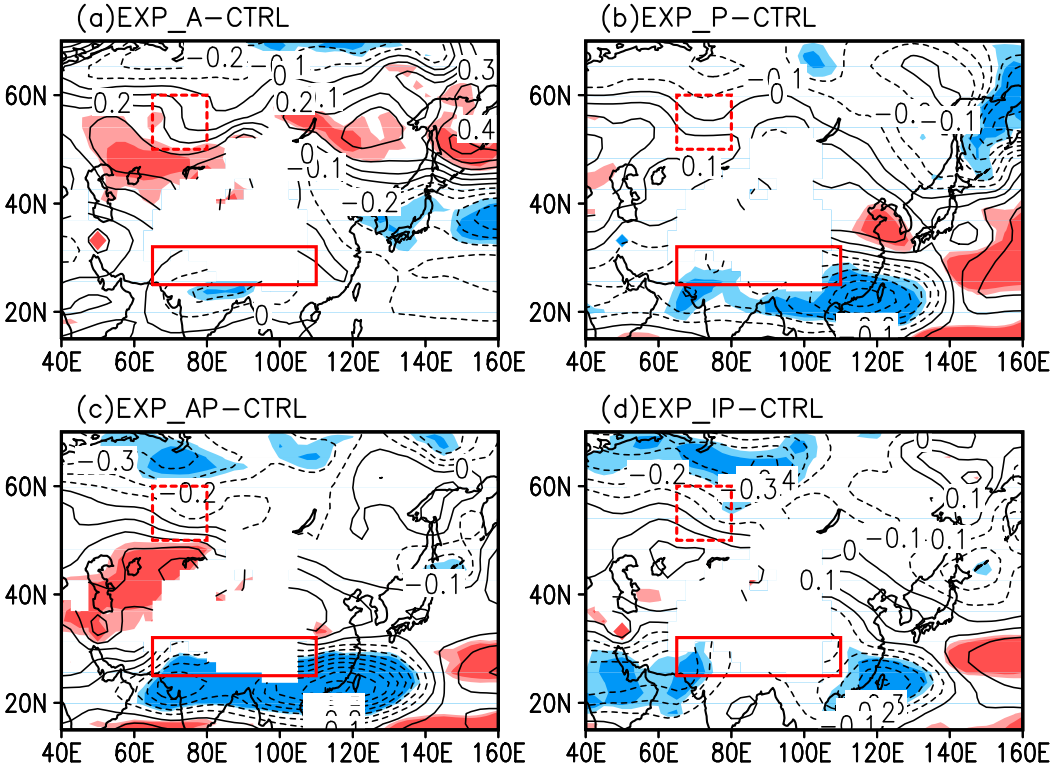

FIG. 16. As in Fig. 14, but for the DJF σ differences (day^{-1}).

The linkage between −IPO +AMO and the shifts of the two jets has been examined by model simulations, focusing on the MTG, baroclinicity, and energetics feedback. In fact, the SST anomalies over the Pacific Ocean and the Atlantic Ocean should affect the atmospheric circulations and therefore impact the variation of MTG and the Eady growth rate. Associated with the SST anomalies over the Pacific Ocean and the Atlantic

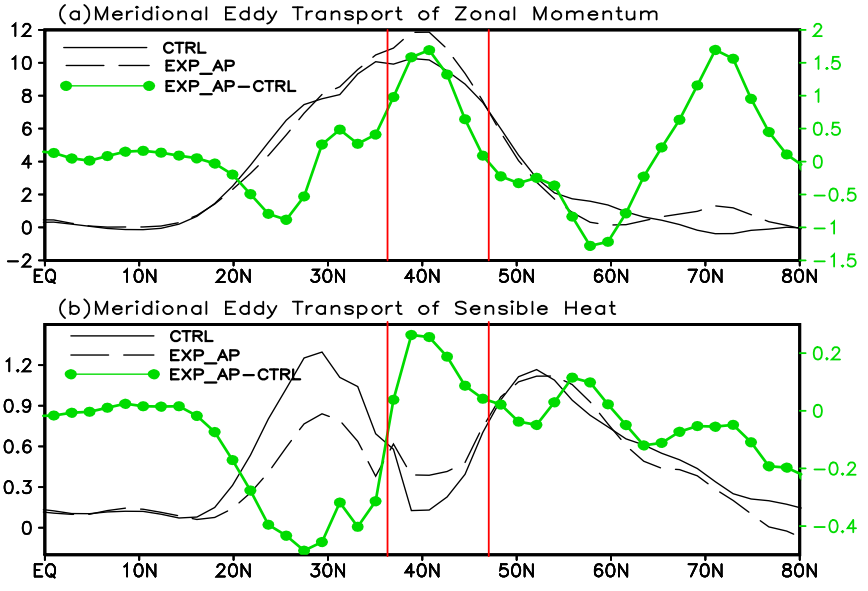

FIG. 17. The 65°–80°E-mean meridional eddy transport of DJF (a) zonal momentum $\overline{u'v'}$ (m^2 s^{-2}) and (b) sensitive heat $\overline{T'v'}$ (K m s^{-1}) in CTRL (solid black line), EXP_AP (dashed black line), and their differences between EXP_AP and CTRL (green line). The vertical red lines indicate the latitude range of regions where the positive wind anomalies occur between EXP_AP and CTRL.

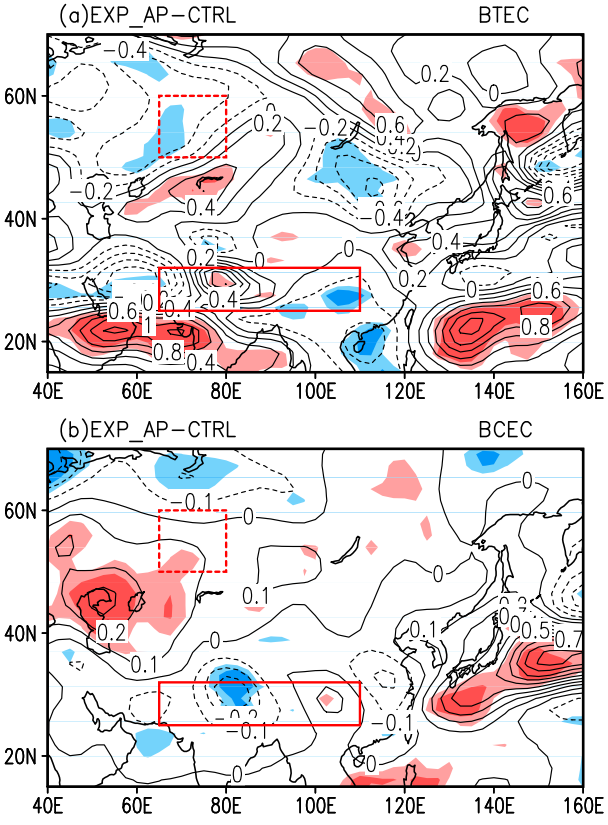

FIG. 18. (a) The 300-hPa DJF BTEC ($W m^{-2}$) and (b) the baroclinic generation from mean available potential energy to eddy available potential energy (BCEC; $W m^{-2}$) differences between EXP_AP and CTRL. The red dashed (solid) box indicates the active region of the EAPJ (EASJ). The light (dark) shading indicates that the difference is significant at the 90% (95%) level based on a Student's *t* test.

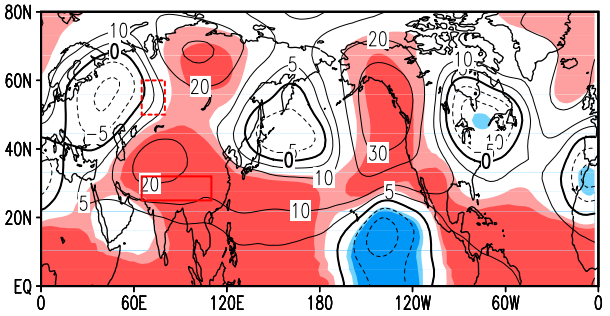

FIG. 19. The 300-hPa DJF geopotential height (gpm) differences between EXP_AP and CTRL. The red dashed (solid) box indicates the active region of the EAPJ (EASJ). The light (dark) shading indicates that the difference is significant at the 90% (95%) level based on a Student's *t* test.

Ocean, a high-pressure anomaly at 300 hPa is located over the region of 20°–40°N, 50°–100°E (Fig. 19), and it may induce an advection of warm and moist air from the south, which would enhance the MTG (Fig. 15c) and increase the baroclinicity (Fig. 16c) around 35°–47.5°N and thus strengthen westerly winds there. We also notice that there is a negative–positive–negative–positive–negative–positive-like wave chain along the latitude band of 40°–60°N, which may be associated with the quasi-stationary waves there. Coumou et al. (2018) recently revealed that in the boreal summer, a weakened equator-to-pole thermal gradient would result in the shifts of the two jets and therefore amplify the quasi-stationary waves. Zhang et al. (1996), Wang et al. (2000), and Luo and Zhang (2015) also proposed that tropical SST anomalies can affect East Asian atmospheric circulations via the Pacific–East Asian teleconnection. Associated with the positive phase of the AMO and through the North Atlantic Oscillation, the Mongolian high over East Asia weakens (Hao and He 2017), which affects the atmospheric circulation over East Asia. More work is still needed to ascertain the teleconnection linkage among the SST variations, the background flow, and the synoptic-scale waves.

Acknowledgments. This study is jointly sponsored by the National Key Research and Development Program of China (Grant 2016YFA0600701), National Natural Science Foundation of China (Grants 41575071 and 41775073), and the Jiangsu Collaborative Innovation Center for Climate Change. Dai acknowledges the funding support from the U.S. National Science Foundation (Grants AGS-1353740 and OISE-1743738), the U.S. Department of Energy's Office of Science (Award DE-SC0012602), and the U.S. National Oceanic and Atmospheric Administration (Award NA15OAR4310086).

REFERENCES

Cai, M., S. Yang, H. M. Van Den Dool, and V. E. Kousky, 2007: Dynamical implications of the orientation of atmospheric eddies: A local energetics perspective. *Tellus*, **59A**, 127–140, https://doi.org/10.1111/j.1600-0870.2006.00213.x.

Chang, E. K. M., and Y. Fu, 2002: Interdecadal variations in Northern Hemisphere winter storm track intensity. *J. Climate*, **15**, 642–658, https://doi.org/10.1175/1520-0442(2002)015<0642:IVINHW>2.0.CO;2.

Compo, G. P., and Coauthors, 2011: The Twentieth Century Reanalysis project. *Quart. J. Roy. Meteor. Soc.*, **137**, 1–28, https://doi.org/10.1002/qj.776.

Coumou, D., G. Di Capua, S. Vavrus, L. Wang, and S. Wang, 2018: The influence of Arctic amplification on mid-latitude summer circulation. *Nat. Commun.*, **9**, 2959, https://doi.org/10.1038/s41467-018-05256-8.

Dai, A., 2013: The influence of the inter-decadal Pacific oscillation on US precipitation during 1923–2010. *Climate Dyn.*, **41**, 633–646, https://doi.org/10.1007/s00382-012-1446-5.

——, J. C. Fyfe, S.-P. Xie, and X. Dai, 2015: Decadal modulation of global surface temperature by internal climate variability. *Nat. Climate Change*, **5**, 555–559, https://doi.org/10.1038/nclimate2605.

Dee, D. P., and Coauthors, 2011: The ERA-Interim reanalysis: Configuration and performance of the data assimilation system. *Quart. J. Roy. Meteor. Soc.*, **137**, 553–597, https://doi.org/10.1002/qj.828.

DeWeaver, E., and S. Nigam, 2000: Do stationary waves drive the zonal-mean jet anomalies of the northern winter? *J. Climate*, **13**, 2160–2176, https://doi.org/10.1175/1520-0442(2000)013<2160:DSWDTZ>2.0.CO;2.

Dong, B., and A. Dai, 2015: The influence of the interdecadal Pacific oscillation on temperature and precipitation over the globe. *Climate Dyn.*, **45**, 2667–2681, https://doi.org/10.1007/s00382-015-2500-x.

——, ——, M. Vuille, and O. Elison Timm, 2018: Asymmetric modulation of ENSO teleconnections by the interdecadal Pacific oscillation. *J. Climate*, **31**, 7337–7361, https://doi.org/10.1175/JCLI-D-17-0663.1.

Dong, L., T. Zhou, A. Dai, F. Song, B. Wu, and X. Chen, 2016: The footprint of the inter-decadal Pacific oscillation in Indian Ocean sea surface temperatures. *Sci. Rep.*, **6**, 21251, https://doi.org/10.1038/srep21251.

Du, Y., Y. Zhang, and Z. Xie, 2009: Impacts of the zonal position of the East Asian westerly jet core on precipitation distribution during meiyu of China. *Acta Meteor. Sin.*, **23**, 506–516.

Eady, E. T., 1949: Long waves and cyclone waves. *Tellus*, **1** (3), 33–52, https://doi.org/10.3402/tellusa.v1i3.8507.

Enfield, D. B., A. M. Mestas-Nuñez, and P. J. Trimble, 2001: The Atlantic multidecadal oscillation and its relation to rainfall and river flows in the continental U.S. *Geophys. Res. Lett.*, **28**, 2077–2080, https://doi.org/10.1029/2000GL012745.

Fuentes-Franco, R., F. Giorgi, E. Coppola, and F. Kucharski, 2016: The role of ENSO and PDO in variability of winter precipitation over North America from twenty first century CMIP5 projections. *Climate Dyn.*, **46**, 3259–3277, https://doi.org/10.1007/s00382-015-2767-y.

Gelaro, R., and Coauthors, 2017: The Modern-Era Retrospective Analysis for Research and Applications, version 2 (MERRA-2). *J. Climate*, **30**, 5419–5454, https://doi.org/10.1175/JCLI-D-16-0758.1.

Hao, X., and S. He, 2017: Combined effect of ENSO-like and Atlantic multidecadal oscillation SSTAs on the interannual variability of the East Asian winter monsoon. *J. Climate*, **30**, 2697–2716, https://doi.org/10.1175/JCLI-D-16-0118.1.

Huang, B., and Coauthors, 2017: Extended Reconstructed Sea Surface Temperature, version 5 (ERSSTv5): Upgrades, validations, and intercomparisons. *J. Climate*, **30**, 8179–8205, https://doi.org/10.1175/JCLI-D-16-0836.1.

Huang, D., M. Takahashi, and Y. Zhang, 2011: Analysis of the baiu precipitation and associated circulations simulated by the MIROC coupled climate system model. *J. Meteor. Soc. Japan*, **89**, 625–636, https://doi.org/10.2151/jmsj.2011-603.

——, J. Zhu, Y. Zhang, and A. Huang, 2014: The different configurations of the East Asian polar front jet and subtropical jet and the associated rainfall anomalies over eastern China in summer. *J. Climate*, **27**, 8205–8220, https://doi.org/10.1175/JCLI-D-14-00067.1.

——, ——, ——, J. Wang, and X. Kuang, 2015: The impact of the East Asian subtropical jet and polar front jet on the frequency of spring persistent rainfall over southern China in 1997–2011. *J. Climate*, **28**, 6054–6066, https://doi.org/10.1175/JCLI-D-14-00641.1.

——, ——, ——, Y. Huang, and X. Kuang, 2016: Assessment of summer monsoon precipitation derived from five reanalysis datasets over East Asia. *Quart. J. Roy. Meteor. Soc.*, **142**, 108–119, https://doi.org/10.1002/qj.2634.

——, A. Dai, J. Zhu, Y. Zhang, and X. Kuang, 2017: Recent winter precipitation changes over eastern China in different warming periods and the associated East Asian jets and oceanic conditions. *J. Climate*, **30**, 4443–4462, https://doi.org/10.1175/JCLI-D-16-0517.1.

Hudson, R., 2012: Measurements of the movement of the jet streams at mid-latitudes, in the Northern and Southern Hemispheres, 1979 to 2010. *Atmos. Chem. Phys.*, **12**, 7797–7808, https://doi.org/10.5194/acp-12-7797-2012.

Joshi, M., and A. Rai, 2015: Combined interplay of the Atlantic multidecadal oscillation and the interdecadal Pacific oscillation on rainfall and its extremes over Indian subcontinent. *Climate Dyn.*, **44**, 3339–3359, https://doi.org/10.1007/s00382-014-2333-z.

Kalnay, E., and Coauthors, 1996: The NCEP/NCAR 40-year reanalysis project. *Bull. Amer. Meteor. Soc.*, **77**, 437–472, https://doi.org/10.1175/1520-0477(1996)077<0437:TNYRP>2.0.CO;2.

Klein, W., 1983: Objective specification of monthly mean surface temperature from mean 700 mb heights in winter. *Mon. Wea. Rev.*, **111**, 674–691, https://doi.org/10.1175/1520-0493(1983)111<0674:OSOMMS>2.0.CO;2.

Knight, J., C. Folland, and A. Scaife, 2006: Climate impacts of the Atlantic multidecadal oscillation. *Geophys. Res. Lett.*, **33**, L17706, https://doi.org/10.1029/2006GL026242.

Kuang, X., and Y. Zhang, 2005: Seasonal variation of the East Asian subtropical westerly jet and its association with the heating field over East Asia. *Adv. Atmos. Sci.*, **22**, 831–840, https://doi.org/10.1007/BF02918683.

——, ——, Y. Huang, and D. Huang, 2014: Spatial differences in seasonal variation of the upper-tropospheric jet stream in the Northern Hemisphere and its thermal dynamic mechanism. *Theor. Appl. Climatol.*, **117**, 103–112, https://doi.org/10.1007/s00704-013-0994-x.

Kug, J., D. Choi, F. Jin, W. Kwon, and H. Ren, 2010: Role of synoptic eddy feedback on polar climate responses to the anthropogenic forcing. *Geophys. Res. Lett.*, **37**, L14704, https://doi.org/10.1029/2010GL043673.

Lee, S. S., 2000: Barotropic effects on atmospheric storm tracks. *J. Atmos. Sci.*, **57**, 1420–1435, https://doi.org/10.1175/1520-0469(2000)057<1420:BEOAST>2.0.CO;2.

——, J. Y. Lee, B. Wang, F. F. Jin, W. J. Lee, and K. J. Ha, 2011: A comparison of climatological subseasonal variations in the wintertime storm track activity between the North Pacific and Atlantic: Local energetics and moisture effect. *Climate Dyn.*, **37**, 2455–2469, https://doi.org/10.1007/s00382-011-1027-z.

——, ——, ——, K. J. Ha, K. Y. Heo, F. F. Jin, D. M. Straus, and J. Shukla, 2012: Interdecadal changes in the storm track activity over the North Pacific and North Atlantic. *Climate Dyn.*, **39**, 313–327, https://doi.org/10.1007/s00382-011-1188-9.

Lehmann, J., D. Coumou, K. Frieler, A. V. Eliseev, and A. Levermann, 2014: Future changes in extratropical storm tracks and baroclinicity under climate change. *Environ. Res. Lett.*, **9**, 084002, https://doi.org/10.1088/1748-9326/9/8/084002.

Li, L., and Y. Zhang, 2014: Effects of different configurations of the East Asian subtropical and polar front jets on precipitation during mei-yu season. *J. Climate*, **27**, 6660–6672, https://doi.org/10.1175/JCLI-D-14-00021.1.

Li, S., Y. Wang, and Y. Hao, 2009: A review of the researches on the Atlantic multidecadal oscillation (AMO) and its climate influence (in Chinese). *Trans. Atmos. Sci.*, **32**, 458–465.

Li, X., J. Li, and Y. Li, 2015: Recent winter precipitation increase in the middle–lower Yangtze River Valley since the late 1970s:

A response to warming in the tropical Indian Ocean. *J. Climate*, **28**, 3857–3879, https://doi.org/10.1175/JCLI-D-14-00701.1.

Liao, Z., and Y. Zhang, 2013: Concurrent variation between the East Asian subtropical jet and polar front jet during persistent snowstorm period in 2008 winter over southern China. *J. Geophys. Res. Atmos.*, **118**, 6360–6373, https://doi.org/10.1002/jgrd.50558.

Liu, Z., 2012: Dynamics of interdecadal climate variability: A historical perspective. *J. Climate*, **25**, 1963–1995, https://doi.org/10.1175/2011JCLI3980.1.

Lu, R., Z. Lin, and Y. Zhang, 2013: Variability of the East Asian upper-tropospheric jet in summer and its impacts on the East Asian monsoon (in Chinese). *Chin. J. Atmos. Sci.*, **37**, 331–340.

Lunkeit, F., K. Fraedrich, and S. E. Bauer, 1998: Storm tracks in a warmer climate: Sensitivity studies with a simplified global circulation model. *Climate Dyn.*, **14**, 813–826, https://doi.org/10.1007/s003820050257.

Luo, X., and Y. Zhang, 2015: The linkage between upper-level jet streams over East Asia and East Asian winter monsoon variability. *J. Climate*, **28**, 9013–9028, https://doi.org/10.1175/JCLI-D-15-0160.1.

Lyu, K., J. Y. Yu, and H. Paek, 2017: The influences of the Atlantic multidecadal oscillation on the mean strength of the North Pacific subtropical high during boreal winter. *J. Climate*, **30**, 411–426, https://doi.org/10.1175/JCLI-D-16-0525.1.

McCabe, G. J., M. A. Palecki, and J. L. Betancourt, 2004: Pacific and Atlantic Ocean influences on multidecadal drought frequency in the United States. *Proc. Natl. Acad. Sci. USA*, **101**, 4136–4141, https://doi.org/10.1073/pnas.0306738101.

Meehl, G. A., A. Hu, J. M. Arblaster, J. Fasullo, and K. E. Trenberth, 2013: Externally forced and internally generated decadal climate variability associated with the interdecadal Pacific oscillation. *J. Climate*, **26**, 7298–7310, https://doi.org/10.1175/JCLI-D-12-00548.1.

——, ——, B. D. Santer, and S.-P. Xie, 2016: Contribution of the interdecadal Pacific oscillation to twentieth-century global surface temperature trends. *Nat. Climate Change*, **6**, 1005–1008, https://doi.org/10.1038/nclimate3107.

Mohino, E., S. Janicot, and J. Bader, 2011: Sahel rainfall and decadal to multi-decadal sea surface temperature variability. *Climate Dyn.*, **37**, 419–440, https://doi.org/10.1007/s00382-010-0867-2.

Neale, R. B., and Coauthors, 2012: Description of the NCAR Community Atmosphere Model (CAM5.0). NCAR Tech. Note NCAR/TN-4861STR, 274 pp., http://www.cesm.ucar.edu/models/cesm1.0/cam/docs/description/cam5_desc.pdf.

Panetta, R., 1993: Zonal jets in wide baroclinically unstable regions: Persistence and scale selection. *J. Atmos. Sci.*, **50**, 2073–2106, https://doi.org/10.1175/1520-0469(1993)050<2073:ZJIWBU>2.0.CO;2.

Power, S., T. Casey, C. Folland, A. Colman, and V. Mehta, 1999: Inter-decadal modulation of the impact of ENSO on Australia. *Climate Dyn.*, **15**, 319–324, https://doi.org/10.1007/s003820050284.

Pui, A., A. Lal, and A. Sharma, 2011: How does the interdecadal Pacific oscillation affect design floods in Australia? *Water Resour. Res.*, **47**, W05554, https://doi.org/10.1029/2010WR009420.

Rayner, N. A., D. E. Parker, E. B. Horton, C. K. Folland, L. V. Alexander, D. P. Rowell, E. C. Kent, and A. Kaplan, 2003: Global analyses of sea surface temperature, sea ice, and night marine air temperature since the late nineteenth century. *J. Geophys. Res.*, **108**, 4407, https://doi.org/10.1029/2002JD002670.

Ren, X., and Y. Zhang, 2007: Western Pacific jet stream anomalies at 200 hPa in winter associated with oceanic surface heating and transient eddy activity. *Acta Meteor. Sin.*, **21**, 277–289.

——, ——, and Y. Xiang, 2008: Connections between wintertime jet stream variability, oceanic surface heating, and transient eddy activity in the North Pacific. *J. Geophys. Res.*, **113**, D21119, https://doi.org/10.1029/2007JD009464.

——, X. Yang, T. Zhou, and J. Fang, 2011: Diagnostic comparison of wintertime East Asian subtropical jet and polar-front jet: Large-scale characteristics and transient eddy activities. *Acta Meteor. Sin.*, **25**, 21–33, https://doi.org/10.1007/s13351-011-0002-2.

Saji, N. H., and T. Yamagata, 2003: Possible impacts of Indian Ocean dipole mode events on global climate. *Climate Res.*, **25**, 151–169, https://doi.org/10.3354/cr025151.

Schiemann, R., D. Lüthi, and C. Schär, 2009: Seasonality and interannual variability of the westerly jet in the Tibetan Plateau region. *J. Climate*, **22**, 2940–2957, https://doi.org/10.1175/2008JCLI2625.1.

Schubert, S., and Coauthors, 2009: A U.S. CLIVAR project to assess and compare the responses of global climate models to drought-related SST forcing patterns: Overview and results. *J. Climate*, **22**, 5251–5272, https://doi.org/10.1175/2009JCLI3060.1.

Seidel, D., Q. Fu, W. Randel, and T. Reichler, 2008: Widening of the tropical belt in a changing climate. *Nat. Geosci.*, **1**, 21–24, https://doi.org/10.1038/ngeo.2007.38.

Si, D., and Y. Ding, 2016: Oceanic forcings of the interdecadal variability in East Asian summer rainfall. *J. Climate*, **29**, 7633–7649, https://doi.org/10.1175/JCLI-D-15-0792.1.

——, ——, and Y. Liu, 2009: Decadal northward shift of the meiyu belt and the possible cause. *Chin. Sci. Bull.*, **54**, 4742–4748, https://doi.org/10.1007/s11434-009-0385-y.

Sutton, R. T., and B. Dong, 2012: Atlantic Ocean influence on a shift in European climate in the 1990s. *Nat. Geosci.*, **5**, 788–792, https://doi.org/10.1038/ngeo1595.

Trenberth, K. E., and D. J. Shea, 2006: Atlantic hurricanes and natural variability in 2005. *Geophys. Res. Lett.*, **33**, L12704, https://doi.org/10.1029/2006GL026894.

——, and J. T. Fasullo, 2013: An apparent hiatus in global warming? *Earth's Future*, **1**, 19–32, https://doi.org/10.1002/2013EF000165.

Wallace, J. M., and P. V. Hobbs, 2005: *Atmospheric Science: An Introductory Survey*. 2nd ed. Elsevier, 483 pp.

Wang, B., R. Wu, and X. Fu, 2000: Pacific–East Asian teleconnection: How does ENSO affect East Asian climate? *J. Climate*, **13**, 1517–1536, https://doi.org/10.1175/1520-0442(2000)013<1517:PEATHD>2.0.CO;2.

Wang, L., R. H. Huang, L. Gu, W. Chen, and L. H. Kang, 2009: Interdecadal variations of the East Asian winter monsoon and their association with quasi-stationary planetary wave activity. *J. Climate*, **22**, 4860–4872, https://doi.org/10.1175/2009JCLI2973.1.

Wang, N., and Y. Zhang, 2015: Connections between the Eurasian teleconnection and concurrent variation of upper-level jets over East Asia. *Adv. Atmos. Sci.*, **32**, 336–348, https://doi.org/10.1007/s00376-014-4088-1.

Xiao, C., and Y. Zhang, 2012: The East Asian upper-tropospheric jet streams and associated transient eddy activities simulated by a climate system model BCC_CSM1.1. *Acta Meteor. Sin.*, **26**, 700–716, https://doi.org/10.1007/s13351-012-0603-4.

——, and ——, 2015: Projected changes of wintertime synoptic-scale transient eddy activities in the East Asian eddy-driven jet from CMIP5 experiments. *Geophys. Res. Lett.*, **42**, 6008–6013, https://doi.org/10.1002/2015GL064641.

Xue, D., and Y. Zhang, 2017: Concurrent variations in the location and intensity of the Asian winter jet streams and the possible

mechanism. *Climate Dyn.*, **49**, 37–52, https://doi.org/10.1007/s00382-016-3325-y.

Yim, B. Y., H. S. Min, and J.-S. Kug, 2016: Inter-model diversity in jet stream changes and its relation to Arctic climate in CMIP5. *Climate Dyn.*, **47**, 235–248, https://doi.org/10.1007/s00382-015-2833-5.

Yu, R., and T. Zhou, 2007: Seasonality and three-dimensional structure of interdecadal change in the East Asian monsoon. *J. Climate*, **20**, 5344–5355, https://doi.org/10.1175/2007JCLI1559.1.

Zhang, L., 2016: The roles of external forcing and natural variability in global warming hiatuses. *Climate Dyn.*, **47**, 3157–3169, https://doi.org/10.1007/s00382-016-3018-6.

Zhang, R., A. Sumi, and M. Kimoto, 1996: Impact of El Niño on the East Asian monsoon: A diagnostic study of the '86/87 and '91/92 events. *J. Meteor. Soc. Japan*, **74**, 49–62, https://doi.org/10.2151/jmsj1965.74.1_49.

Zhang, Y., and D. Huang, 2011: Has the East Asian westerly jet experienced a poleward displacement in recent decades? *Adv. Atmos. Sci.*, **28**, 1259–1265, https://doi.org/10.1007/s00376-011-9185-9.

——, D. Wang, and X. Ren, 2008: Seasonal variation of the meridional wind in the temperate jet stream and its relationship to the Asian monsoon. *Acta Meteor. Sin.*, **22**, 446–454.

Zhu, J., D. Q. Huang, Y. C. Zhang, A. N. Huang, X. Y. Kuang, and Y. Huang, 2013: Decadal changes of meiyu rainfall around 1991 and its relationship with two types of ENSO. *J. Geophys. Res. Atmos.*, **118**, 9766–9777, https://doi.org/10.1002/jgrd.50779.

——, ——, Y. Dai, and X. Chen, 2016: Recent heterogeneous warming and the associated summer precipitation over eastern China. *Theor. Appl. Climatol.*, **123**, 619–627, https://doi.org/10.1007/s00704-015-1380-7.

——, ——, P. Yan, Y. Huang, and X. Kuang, 2017: Can reanalysis datasets describe the persistent temperature and precipitation extremes over China? *Theor. Appl. Climatol.*, **130**, 655–671, https://doi.org/10.1007/s00704-016-1912-9.

Zhu, Y., H. Wang, J. Ma, T. Wang, and J. Sun, 2015: Contribution of the phase transition of Pacific decadal oscillation to the late 1990s' shift in East China summer rainfall. *J. Geophys. Res. Atmos.*, **120**, 8817–8827, https://doi.org/10.1002/2015JD023545.

Zou, J. S., J. Jing, and M. H. Wang, 1990: *Climatology in the Upper Atmosphere* (in Chinese). China Meteorological Press, 212 pp.